

Snowflake Point Deconvolution for Point Cloud Completion and Generation With Skip-Transformer

Peng Xiang, Xin Wen[✉], Yu-Shen Liu[✉], Member, IEEE, Yan-Pei Cao[✉], Pengfei Wan[✉], Wen Zheng, and Zhizhong Han

Abstract—Most existing point cloud completion methods suffer from the discrete nature of point clouds and the unstructured prediction of points in local regions, which makes it difficult to reveal fine local geometric details. To resolve this issue, we propose SnowflakeNet with snowflake point deconvolution (SPD) to generate complete point clouds. SPD models the generation of point clouds as the snowflake-like growth of points, where child points are generated progressively by splitting their parent points after each SPD. Our insight into the detailed geometry is to introduce a skip-transformer in the SPD to learn the point splitting patterns that can best fit the local regions. The skip-transformer leverages attention mechanism to summarize the splitting patterns used in the previous SPD layer to produce the splitting in the current layer. The locally compact and structured point clouds generated by SPD precisely reveal the structural characteristics of the 3D shape in local patches, which enables us to predict highly detailed geometries. Moreover, since SPD is a general operation that is not limited to completion, we explore its applications in other generative tasks, including point cloud auto-encoding, generation, single image reconstruction, and upsampling. Our experimental results outperform state-of-the-art methods under widely used benchmarks.

Index Terms—Point clouds, 3D shape completion, generation, reconstruction, upsampling, transformer

1 INTRODUCTION

In 3D computer vision [1], [2], [3], [4] applications, raw point clouds captured by 3D scanners and depth cameras are usually sparse and incomplete [5], [6], [7] due to occlusion and limited sensor resolution. Therefore, point cloud completion [5], [8], which aims to predict a complete shape from its partial observation, is vital for various downstream tasks. Benefiting from large-scale point cloud datasets, deep learning-based point cloud completion methods have

attracted more research interest. Current methods either constrain the generation of point clouds using a hierarchical rooted tree structure [8], [9], [10] or assume a specific topology [5], [11] for the target shape. However, most of these methods suffer from the discrete nature of point clouds and the unstructured prediction of points in local regions, which makes it difficult to preserve a well-arranged structure for points in local patches. Therefore, it is still challenging to reveal the local geometric details and structure characteristics, such as smooth regions, sharp edges, and corners, while completing partial 3D shapes, as illustrated in Fig. 1.

To address this problem, we propose a novel network called *SnowflakeNet* that focuses primarily on the decoding process to complete partial point clouds. *SnowflakeNet* mainly consists of layers of *snowflake point deconvolution* (SPD), which models the generation of complete point clouds like the snowflake growth of points in 3D space. We progressively generate points by stacking one SPD layer upon another. Each SPD layer produces child points by splitting their parent point while inheriting the shape characteristics captured by the parent point. Fig. 2 illustrates the process of SPD and point-wise splitting.

Our insight into the detailed geometry is to introduce a *skip-transformer* in SPD to learn the point splitting patterns that can best fit the local regions. Compared with the previous methods, which often ignore the spatial relationship among points [8], [11], [13] or merely learn through self-attention in a single level of multi-step point cloud decoding [5], [9], [14], our proposed skip-transformer integrates the spatial relationships across different decoding levels. Therefore, it can establish a cross-level spatial relationship

• Peng Xiang is with the School of Software, Tsinghua University, Beijing 100190, China. E-mail: xp20@mails.tsinghua.edu.cn.

• Xin Wen is with the School of Software, Tsinghua University, Beijing 100190, China, and also with JD.com, Beijing 101111, China. E-mail: x-wen16@mails.tsinghua.edu.cn.

• Yu-Shen Liu is with the School of Software, BNRist, Tsinghua University, Beijing 100190, China. E-mail: liuyushen@tsinghua.edu.cn.

• Yan-Pei Cao is with ARC Lab, Tencent PCG, 100084, China. E-mail: caoyanpei@gmail.com.

• Pengfei Wan and Wen Zheng are with Y-Tech, Kuaishou Technology, Beijing 100085, China. E-mail: {wanpengfei, zhengwen}@kuaishou.com.

• Zhizhong Han is with the Department of Computer Science, Wayne State University, Detroit, MI 48202 USA. E-mail: h312h@wayne.edu.

Manuscript received 5 December 2021; revised 1 October 2022; accepted 16 October 2022. Date of publication 25 October 2022; date of current version 3 April 2023.

This work was supported in part by National Key R&D Program of China under Grants 2022YFC3800600 and 2020YFF0304100, in part by the National Natural Science Foundation of China under Grants 62272263 and 62072268, and in part by the Tsinghua-Kuaishou Institute of Future Media Data.

(Corresponding author: Yu-Shen Liu.)

Recommended for acceptance by E. Kalogerakis.

This article has supplementary downloadable material available at <https://doi.org/10.1109/TPAMI.2022.3217161>, provided by the authors.

Digital Object Identifier no. 10.1109/TPAMI.2022.3217161

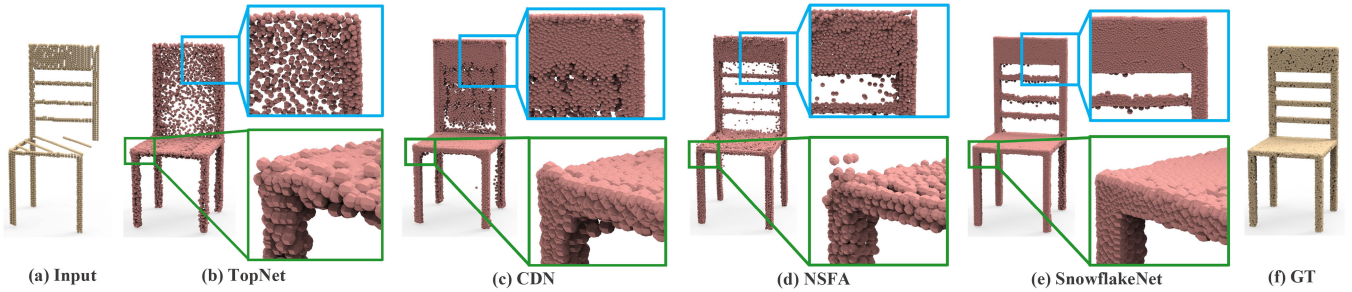


Fig. 1. Visual comparison of point cloud completion results. The input and ground truth have 2048 and 16384 points, respectively. Compared with the current completion methods such as TopNet [8], CDN [9], and NSFA [12], our SnowflakeNet can generate the complete shape (16384 points) with fine-grained geometric details, such as smooth regions (blue boxes), sharp edges, and corners (green boxes).

between points in different decoding steps and refine their locations to produce a more detailed structure. To achieve this, the skip-transformer leverages the attention mechanism to summarize the splitting patterns used in the previous SPD layer, with the aim of producing splitting in the current SPD layer. The skip-transformer can learn the shape context and the spatial relationship between the points in local patches. This enables the network to precisely capture the structural characteristics in local patches and predict a higher quality point cloud for both smooth planes and sharp edges in 3D space. We achieved state-of-the-art completion accuracy under widely used benchmarks. Furthermore, SPD is a general operation for point cloud generation that is simple and effective. We take a step forward and explore its performance in more tasks that are closely related to point cloud generation, including point cloud auto-encoding, novel point cloud generation, single image reconstruction, and point cloud upsampling. The generalization ability of SPD is demonstrated by quantitative and qualitative results in our experiments.

Our main contributions can be summarized as follows.

- We propose a novel SnowflakeNet for point cloud completion. Compared with previous methods that do not consider local generation patterns, SnowflakeNet can interpret point cloud completion as an explicit and structured local pattern generation that effectively improves the performance of 3D shape completion.

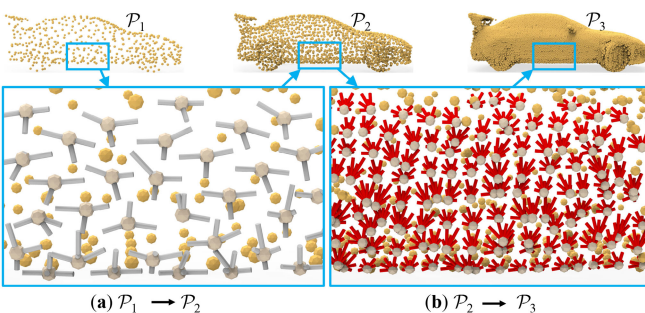


Fig. 2. Illustration of snowflake point deconvolution (SPD) for completing missing parts of a car. To show the local changes more clearly, we only illustrate some sample points as parent points in the same patch and demonstrate their splitting paths for child points, which are marked as gray and red lines, respectively. (a) illustrates the SPD of point splitting from a coarse point cloud P_1 (512 points) to its splitting P_2 (2048 points). (b) illustrates the SPD of point splitting from P_2 to complete and dense point cloud P_3 (16384 points), where the child points are expanding like the growing process of snowflakes.

- We propose the novel snowflake point deconvolution (SPD) for progressively increasing the number of points. It reformulates the generation of child points from parent points as a snowflake growing process, where the shape characteristics embedded in the parent point features are extracted and inherited by the child points through a *point-wise splitting* operation.
- We introduce a novel skip-transformer to learn the splitting patterns in SPD. It learns the shape context and spatial relationship between child points and parent points. This process encourages SPD to produce locally structured and compact point arrangements and captures the structural characteristics of 3D surfaces in local patches.
- In addition to point cloud completion, we further generalize SPD to more tasks related to point cloud generation. With a few network arrangements, SPD can be well applied to multiple point cloud generation scenarios. Comprehensive experiments are conducted to verify the effectiveness and generation ability of SPD.

2 RELATED WORK

2.1 Point Cloud Completion

Point cloud completion methods can be roughly divided into two categories. (1) Traditional point cloud completion methods [15], [16], [17], [18] usually assume that the 3D shape has a smooth surface or utilize a large-scaled complete shape dataset to infer the missing regions for incomplete shapes. (2) Deep learning-based methods [9], [19], [20], [21], [22], [23], [24], [25], [26], [27], [28], [29], [30], [31], [32], [33], [34], [35], [36], [37], [38], [39], [40], [41], [42], [43], [44], however, learn to predict a complete shape based on the prior of the training data. Our method falls into the second category and focuses on the decoding process of point cloud completion. We briefly review deep learning-based methods below.

Point Cloud Completion by Folding-Based Decoding. The development of deep learning-based 3D point cloud processing techniques [45], [46], [47], [48], [49], [50], [51], [52], [53], [54] has boosted the research of point cloud completion. Due to the discrete nature of point cloud data, the generation of high-quality complete shapes is one of the major concerns in point cloud completion research. One of the pioneering works is FoldingNet [11], which is proposed for point cloud

generation rather than completion. It includes a two-stage generation process and combines the assumption that the 3D object lies on a 2D-manifold [8]. Following a similar practice, methods such as SA-Net [5] further extended this type of generation process into multiple stages by proposing hierarchical folding in the decoder. However, the problem with these folding-based methods [5], [11], [55], [56] is that the 3-dimensional code generated by intermediate layer of the network is an implicit representation of the target shape, which cannot be interpreted or constrained to help refine the shape in the local region. On the other hand, TopNet [8] modeled the point cloud generation process as the growth of a rooted tree, where one parent point feature is projected into several child point features in a feature expansion layer. Similar to FoldingNet [11], the intermediate generation processes of TopNet and SA-Net are also implicit, where the shape information is only represented by the point features and cannot be constrained or explicitly explained.

Point Cloud Completion by Coarse-to-Fine Decoding. Recently, the explicit coarse-to-fine completion framework [10], [57], [58], [59], [60] has received increasing attention, due to its explainable nature and controllable generation process. Typical methods such as PCN [61] and NSFA [12] adopted the two-stage generation framework, where a coarse and low-resolution point cloud is first generated by the decoder, and then a lifting module is used to increase the density of point clouds. Such methods can achieve better performance since they can impose more constraints on the generation process of point clouds, i.e., coarse one and the dense one. Followers like CDN [9] and PF-Net [19] further extended the number of generation stages and achieved the current state-of-the-art performance. Although intriguing performance has been achieved by the studies along this line, most of these methods still cannot preserve a locally structured point splitting pattern, as illustrated in Fig. 1. The biggest problem is that these methods only focus on the expansion of the point number and the reconstruction of the global shape, while failing to preserve a well-structured generation process for points in local regions. This makes it difficult for these methods to capture the local detailed geometries and structures of 3D shapes.

Compared with the above methods, our SnowflakeNet takes one step further to explore an explicit, explainable and locally structured solution for generating complete point clouds. SnowflakeNet models the progressive generation of point clouds as a hierarchical rooted tree structure like TopNet, while keeping the process explainable and explicit like CDN [9] and PF-Net [19]. Moreover, it excels over the predecessors by arranging the point splitting in local regions in a locally structured pattern, which enables the precise capture of the detailed geometries and structures of 3D shapes.

2.2 Point Cloud Generation

In addition to point cloud completion, improvements in 3D point cloud representation learning have significantly stimulated the progress of point cloud generation. Different generative tasks for point clouds can be categorized by the forms of inputs, such as point cloud auto-encoding, point cloud upsampling, single image reconstruction, and novel point cloud generation.

The task of point cloud auto-encoding [11], [62] aims to learn discriminative representations by encoding the input point cloud into a bottleneck latent code and then reconstructing the point cloud itself from the compact code. Auto-encoding is also commonly used to evaluate the performance of generative decoders [63], [64]. FoldingNet [11] is one of the pioneering works that attempts to generate point clouds by transforming regular 2D grids into 3D shape surfaces. AtlasNet [62] takes a step further and uses multiple sets of 2D grids to fit different regions of the underlying shape.

Point cloud upsampling [14], [65] also consumes point clouds, but the inputs are often sparse and nonuniformly distributed, so the target is to generate dense point clouds with the points faithfully and uniformly located on the underlying surface. One of the representative works in this area is PU-GAN [55], which leverages a generative adversarial network to bridge the gap between sparse point clouds and dense outputs. More recently, PU-GCN [66] proposed a novel graph convolution network to facilitate upsampling by encoding robust local information. DisPU [67] proposes a two-step network to disentangle the targets of upsampling and refinement and achieves credible performance.

The task of single image (view) reconstruction takes a single image as input and aims to generate the underlying point cloud with high quality. Earlier works such as PSGN [68] and AtlasNet [62] attempt to generate point clouds from images through convolution and MLP-based architectures. Recently, 3DAttrFlow [69] proposed assigning disentangled semantic attributes to 3D point clouds by combining an attribute flow pipe and a deformation pipe, which achieves state-of-the-art performance in single image reconstruction.

In addition to deterministic data forms such as point clouds and images, the input can also be a randomly sampled latent code from a probabilistic distribution, which leads to novel shape generation [70], [71], [72]. To generate point clouds with diverse shapes and good quality, many methods have been explored from diverse perspectives. PointFlow [64] leverages continuous normalizing flow to achieve the transformation from the sampled point distribution to the target. ShapeGF [73] moves points to the target position by learning gradient fields. More recently, DPM [63] takes inspiration from non-equilibrium thermodynamics and conducts point cloud generation through a Markov chain [63].

Despite the different forms of inputs, point cloud generation aims to produce high-quality shapes with detailed geometries. Although decent progress has been made in individual tasks, effective generative operations that can be conveniently applied to different tasks are necessary. Therefore, in this paper, we extend snowflake point deconvolution (SPD) to multiple generative tasks, including point cloud auto-encoding, novel point cloud generation, single image reconstruction, and point cloud upsampling.

2.3 Relation to Transformer

The transformer [74] was initially proposed for encoding sentences in natural language processing, but soon became

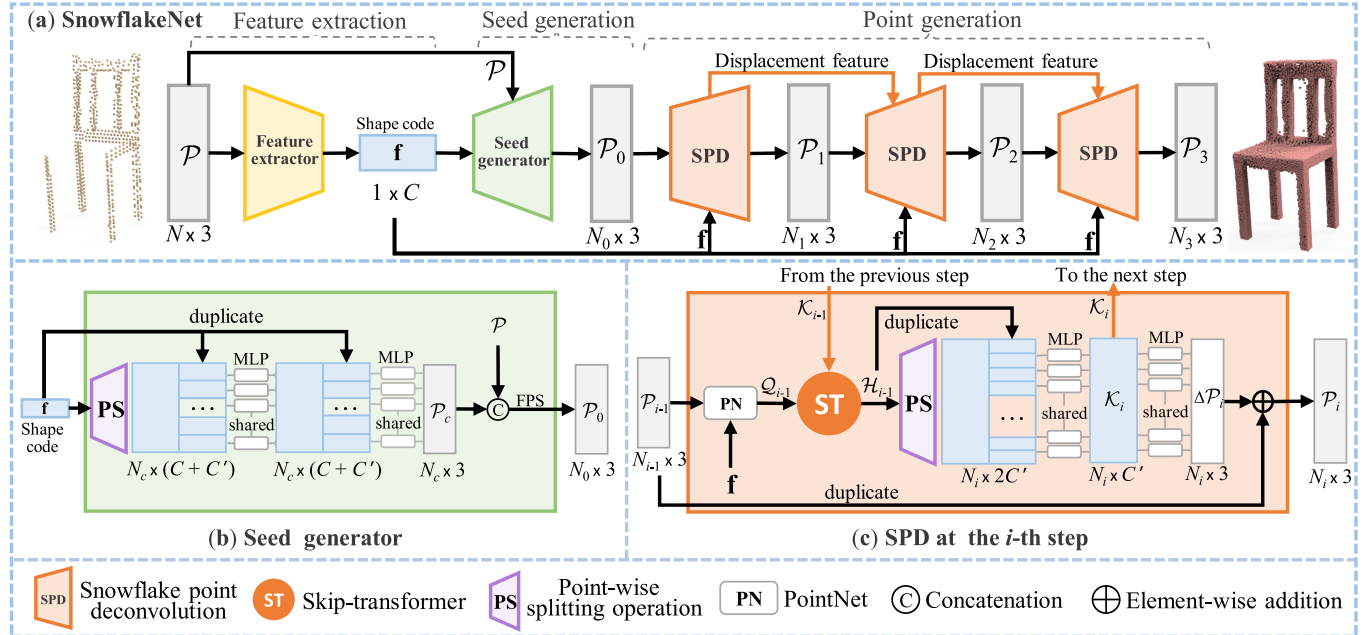


Fig. 3. (a) The overall architecture of SnowflakeNet, which consists of the following three modules: feature extraction, seed generation and point generation. (b) The details of the seed generation module. (c) Snowflake point deconvolution (SPD). Note that N , N_c , and N_i are the numbers of points, and C and C' are the numbers of point feature channels, which are 512 and 128, respectively.

popular in the research of 2D computer vision (CV) [75], [76]. Then, the success of transformer-based 2D CV studies drew the attention of 3D point cloud research, where pioneering studies such as Point Transformer [77], PCT [78], and Pointformer [79] have introduced such framework in the encoding process of point clouds to learn the representation. In our work, instead of only utilizing its representation learning ability, we further extend the application of transformer-based structure into the decoding process of point cloud completion, and reveal its ability to generate high-quality 3D shapes through the proposed skip-transformer.

3 SNOWFLAKE NET

The overall architecture of SnowflakeNet, which is shown in Fig. 3a, consists of the following three modules: feature extraction, seed generation, and point generation. We will detail each module in the following.

3.1 Overview

Feature Extraction Module. Let $\mathcal{P} = \{\mathbf{p}_j\}$ with a size of $N \times 3$ be an input point cloud, where N is the number of points and each point \mathbf{p}_j indicates a 3D coordinate. The feature extractor aims to extract a shape code \mathbf{f} with a size of $1 \times C$, which captures the global structure and detailed local pattern of the target shape. To achieve this, we adopt three layers of set abstraction from [81] to aggregate point features from local to global, along which point transformer [77] is applied to incorporate the local shape context.

Seed Generation Module. The objective of the seed generator is to produce a coarse but complete point cloud \mathcal{P}_0 with a size of $N_0 \times 3$ that captures the geometry and structure of the target shape. As shown in Fig. 3b, with the extracted shape code \mathbf{f} , the seed generator first produces point features that capture both the existing and missing structures through the point-wise splitting operation. Next, the per-

point features are integrated with the shape code through a multi-layer perceptron (MLP) to generate a coarse point cloud \mathcal{P}_c of size $N_c \times 3$. Then, following the previous method [9], \mathcal{P}_c is merged with the input point cloud \mathcal{P} by concatenation, and then the merged point cloud is down-sampled to \mathcal{P}_0 through farthest point sampling (FPS) [81]. In this paper, we typically set $N_c = 256$ and $N_0 = 512$, where a sparse point cloud \mathcal{P}_0 suffices for representing the underlying shape. \mathcal{P}_0 will serve as the seed point cloud for point generation module.

Point Generation Module. The point generation module consists of three snowflake point deconvolution (SPD) steps, each of which takes the point cloud from the previous step as input and splits it by upsampling factors (denoted by r_1, r_2 , and r_3) to obtain $\mathcal{P}_1, \mathcal{P}_2$, and \mathcal{P}_3 , which have the point sizes of $N_1 \times 3, N_2 \times 3$, and $N_3 \times 3$. The SPDs collaborate to generate a rooted tree structure that complies with the local pattern for every seed point. The SPD structure is detailed below.

3.2 Snowflake Point Deconvolution (SPD)

Motivation. The SPD aims to increase the number of points and reveal the detailed geometry in local regions. This is achieved by multiple steps of point splitting, from which a tree-structured local patch is generated for each seed point. To ensure that the patch can best fit the local region, the following two goals must be achieved in each splitting step: (1) capture the local geometric pattern and (2) transfer the captured geometric information to the child features during splitting. To aggregate accurate local geometric patterns, self-attention is a simple and intuitive solution. In multi-step point splitting, however, self-attention will not suffice because it only considers the context in the current step but ignores the historic splitting information, thus may fail to arrange the multi-step splitting in an organized way. To

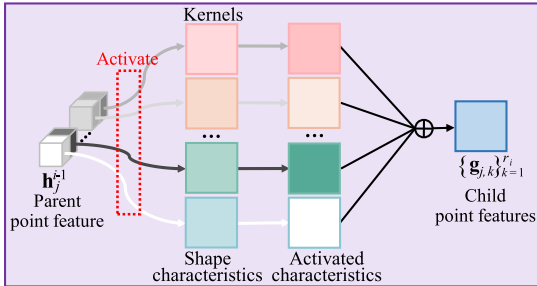


Fig. 4. The point-wise splitting operation. The cubes are logits of the parent point feature that represent the activation status of the corresponding shape characteristics (Kernels), and the child point features are obtained by adding activated shape characteristics.

address this issue, we propose a skip-transformer to enable collaboration between SPDs. While the skip-transformer benefits from the attention mechanism and can well capture the local context, it can also adjust the splitting pattern in consecutive SPDs. After capturing the local geometric pattern, child features can be obtained by first duplicating the parent features and then adding variations. Existing methods [9], [12], [61] usually adopt the folding-based strategy [11] to obtain the variations, which is used for learning different displacements for the duplicated points. However, the folding operation samples the same 2D grids for each parent point and ignores the local shape characteristics contained in the parent point. In contrast, the SPD obtains variations through a *point-wise splitting* operation, which fully leverages the geometric information in parent points and adds variations that comply with local patterns.

Fig. 3c illustrates the structure of the i th SPD with upsampling factor r_i . We denote a set of parent points obtained from the previous step as $\mathcal{P}_{i-1} = \{\mathbf{p}_j^{i-1}\}_{j=1}^{N_{i-1}}$. We split the parent points in \mathcal{P}_{i-1} by duplicating them r_i times to generate a set of child points $\hat{\mathcal{P}}_i$ and then spreading $\hat{\mathcal{P}}_i$ to the neighborhood of the parent points. To achieve this, we take the inspiration from [61] to predict the *point displacement* $\Delta\mathcal{P}_i$ of $\hat{\mathcal{P}}_i$. Then, $\hat{\mathcal{P}}_i$ is updated as $\mathcal{P}_i = \hat{\mathcal{P}}_i + \Delta\mathcal{P}_i$, where \mathcal{P}_i is the output of the i th SPD.

In detail, taking the shape code \mathbf{f} from feature extraction, the SPD first extracts the per-point feature $\mathcal{Q}_{i-1} = \{\mathbf{q}_j^{i-1}\}_{j=1}^{N_{i-1}}$ for \mathcal{P}_{i-1} by adopting the basic PointNet [81] framework. Then, \mathcal{Q}_{i-1} is sent to the skip-transformer to learn the *shape context feature*, denoted as $\mathcal{H}_{i-1} = \{\mathbf{h}_j^{i-1}\}_{j=1}^{N_{i-1}}$. Next, \mathcal{H}_{i-1} is upsampled by a *point-wise splitting* operation and duplication, respectively, where the former serves to add variations and the latter preserves shape context information. Finally, the upsampled feature with a size of $N_i \times 2 C'$ is fed to MLP to produce the *displacement feature* $\mathcal{K}_i = \{\mathbf{k}_j^i\}_{j=1}^{N_i}$ of the current step. Here, \mathcal{K}_i is used for generating the point displacement $\Delta\mathcal{P}_i$, and will be fed into the next SPD. $\Delta\mathcal{P}_i$ is formulated as follows:

$$\Delta\mathcal{P}_i = \tanh(\text{MLP}(\mathcal{K}_i)), \quad (1)$$

where \tanh is the hyper-tangent activation.

Point-Wise Splitting Operation. The point-wise splitting operation aims to generate multiple child point features for each $\mathbf{h}_j^{i-1} \in \mathcal{H}_{i-1}$. Fig. 4 shows this operation structure used in the i th SPD (see Fig. 3c). It is a special one-dimensional deconvolution strategy, where the kernel size and stride are

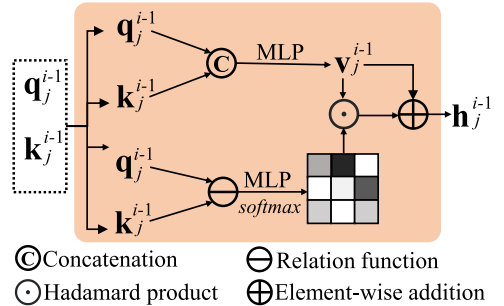


Fig. 5. The detailed structure of the skip-transformer.

equal to r_i . In practice, each $\mathbf{h}_j^{i-1} \in \mathcal{H}_{i-1}$ shares the same set of kernels and produces multiple child point features in a point-wise manner. To be clear, we denote the m th logit of \mathbf{h}_j^{i-1} as $h_{j,m}^{i-1}$, and its corresponding kernel is indicated by K_m . Technically, K_m is a matrix with a size of $r_i \times C'$, the k th row of K_m is denoted as $\mathbf{k}_{m,k}$, and the k th child point feature $\mathbf{g}_{j,k}$ is given by

$$\mathbf{g}_{j,k} = \sum_m h_{j,m}^{i-1} \mathbf{k}_{m,k}. \quad (2)$$

In addition, in Fig. 4, we assume that each learnable kernel K_m indicates a certain shape characteristic, which describes the geometries and structures of the 3D shapes in local regions. Correspondingly, every logit $h_{j,m}^{i-1}$ indicates the activation status of the m th shape characteristic. The child point features can be generated by adding the activated shape characteristics. Moreover, the point-wise splitting operation is flexible for upsampling points. For example, when $r_i = 1$, the SPD can move the point from the previous step to a better position; when $r_i > 1$, it serves to expand the number of points by a factor of r_i .

Collaboration Between SPDs. In Fig. 3a, we adopt three SPDs to generate the complete point cloud. We first set the upsampling factor $r_1 = 1$ to explicitly rearrange the seed point positions. Then, we set $r_2 > 1$ and $r_3 > 1$ to generate a structured tree for every point in \mathcal{P}_1 . Collaboration between SPDs is crucial for coherently growing the tree, because the information from the previous splitting step can be used to guide the current step. In addition, the growth of the rooted trees should also capture the pattern of local patches to keep them from overlapping with each other. To achieve this, we propose a novel *skip-transformer* to serve as the cooperation unit between SPDs. In Fig. 5, the skip-transformer takes per-point feature \mathbf{q}_j^{i-1} as input, and combines it with displacement feature \mathbf{k}_j^{i-1} from the previous step to produce the shape context feature \mathbf{h}_j^{i-1} , which is given by

$$\mathbf{h}_j^{i-1} = \text{ST}(\mathbf{k}_j^{i-1}, \mathbf{q}_j^{i-1}), \quad (3)$$

where ST denotes the skip-transformer. The detailed structure is described as follows.

3.3 Skip-Transformer

Fig. 5 shows the structure of skip-transformer. The skip-transformer is introduced to learn and refine the spatial context between the parent points and their child points, where the term “skip” represents the connection between the

displacement feature from the previous layer and the point feature of the current layer.

Given per-point feature \mathbf{q}_j^{i-1} and displacement feature \mathbf{k}_j^{i-1} , the skip-transformer first concatenates them. Then, the concatenated feature is fed to MLP, which generates the vector \mathbf{v}_j^{i-1} . Here, \mathbf{v}_j^{i-1} serves as the value vector which incorporates previous point splitting information. To further aggregate local shape context into \mathbf{v}_j^{i-1} , the skip-transformer uses \mathbf{q}_j^{i-1} as the query and \mathbf{k}_j^{i-1} as the key to estimate attention vector \mathbf{a}_j^{i-1} , where \mathbf{a}_j^{i-1} denotes how much attention the current splitting should pay to the previous one. To enable the skip-transformer to concentrate on local patterns, we calculate attention vectors between each point and its k -nearest neighbors (k -NN). The k -NN strategy also helps to reduce the computational cost. Specifically, given the j th point feature \mathbf{q}_j^{i-1} , the attention vector $\mathbf{a}_{j,l}^{i-1}$ between \mathbf{q}_j^{i-1} and the displacement features of the k -nearest neighbors $\{\mathbf{k}_{j,l}^{i-1} | l = 1, 2, \dots, k\}$ can be calculated as follows:

$$\mathbf{a}_{j,l}^{i-1} = \frac{\exp(\text{MLP}((\mathbf{q}_j^{i-1}) \ominus (\mathbf{k}_{j,l}^{i-1})))}{\sum_{l=1}^k \exp(\text{MLP}((\mathbf{q}_j^{i-1}) \ominus (\mathbf{k}_{j,l}^{i-1}))), \quad (4)$$

where \ominus is the relation operation, i.e., elementwise subtraction. Finally, the shape context feature \mathbf{h}_j^{i-1} can be obtained by

$$\mathbf{h}_j^{i-1} = \mathbf{v}_j^{i-1} \oplus \sum_{l=1}^k \mathbf{a}_{j,l}^{i-1} \odot \mathbf{v}_{j,l}^{i-1}, \quad (5)$$

where \oplus denotes an elementwise addition and \odot is Hadamard product. Note that there is no previous displacement feature for the first SPD, of which the skip-transformer takes \mathbf{q}_j^0 as both the query and key.

3.4 Training Loss

3.4.1 Completion Loss

We leverage the Chamfer distance (CD) or Earth Mover's distance (EMD) as the primary loss function. The L_2 version of the Chamfer distance (CD) is defined as follows:

$$\mathcal{L}_{\text{CD}_2}(\mathcal{X}, \mathcal{Y}) = \sum_{\mathbf{x} \in \mathcal{X}} \min_{\mathbf{y} \in \mathcal{Y}} \|\mathbf{x} - \mathbf{y}\|_2 + \sum_{\mathbf{y} \in \mathcal{Y}} \min_{\mathbf{x} \in \mathcal{X}} \|\mathbf{y} - \mathbf{x}\|_2, \quad (6)$$

where \mathcal{X} and \mathcal{Y} are point sets, $\mathbf{x} \in \mathcal{X}$ and $\mathbf{y} \in \mathcal{Y}$ are point coordinates, respectively. The L_1 version of CD replaces L_2 -norm in Eq. (6) with L_1 -norm and divide by 2, which is given as

$$\mathcal{L}_{\text{CD}_1}(\mathcal{X}, \mathcal{Y}) = \frac{1}{2} \sum_{\mathbf{x} \in \mathcal{X}} \min_{\mathbf{y} \in \mathcal{Y}} \|\mathbf{x} - \mathbf{y}\| + \frac{1}{2} \sum_{\mathbf{y} \in \mathcal{Y}} \min_{\mathbf{x} \in \mathcal{X}} \|\mathbf{y} - \mathbf{x}\|. \quad (7)$$

To explicitly constrain point clouds generated in the seed generation and the subsequent splitting process, we downsample the ground truth point clouds to the same sampling density as $\{\mathcal{P}_c, \mathcal{P}_1, \mathcal{P}_2, \text{ and } \mathcal{P}_3\}$ (see Fig. 3). We define the sum of the four CD losses as the *completion loss*, denoted as follows:

$$\mathcal{L}_{\text{completion}} = \mathcal{L}_{\text{CD}}(\mathcal{P}_c, \mathcal{P}'_c) + \sum_{i=1}^3 \mathcal{L}_{\text{CD}}(\mathcal{P}_i, \mathcal{P}'_i), \quad (8)$$

where \mathcal{P}'_i and \mathcal{P}'_c denote the down-sampled ground truth point clouds that have the same point number as point cloud \mathcal{P}_i and \mathcal{P}_c , respectively.

Meanwhile, we also follow MSN [13] and SpareNet [32] to take the Earth Mover's distance (EMD) as training loss, which is defined as follows:

$$\mathcal{L}_{\text{EMD}} = \min_{\phi: \mathcal{X} \rightarrow \mathcal{Y}} \sum_{\mathbf{x} \in \mathcal{X}} \|\mathbf{x} - \phi(\mathbf{x})\|_2, \quad (9)$$

where ϕ is a bijection mapping: $\phi: \mathcal{X} \rightarrow \mathcal{Y}$. To take EMD as *completion loss*, we replace the \mathcal{L}_{CD} in Equation (8) with \mathcal{L}_{EMD} .

3.4.2 Preservation Loss

We exploit the *partial matching loss* from [7] to preserve the shape structure of the incomplete point cloud, which is defined as

$$\mathcal{L}_{\text{partial}}(\mathcal{X}, \mathcal{Y}) = \sum_{\mathbf{x} \in \mathcal{X}} \min_{\mathbf{y} \in \mathcal{Y}} \|\mathbf{x} - \mathbf{y}\|_2. \quad (10)$$

The partial matching loss is a unidirectional constraint that aims to match one shape to the other without constraining the opposite direction. Because the partial matching loss only requires the output point cloud to partially match the input, we take it as the *preservation loss* $\mathcal{L}_{\text{preservation}}$, and the total training loss is formulated as follows:

$$\mathcal{L} = \mathcal{L}_{\text{completion}} + \lambda \mathcal{L}_{\text{preservation}}, \quad (11)$$

where we typically set $\lambda = 1$.

4 EXPERIMENTS

To comprehensively justify the effectiveness of our SnowflakeNet, we first conduct comprehensive experiments under two widely used benchmarks: PCN [61] and Completion3D [8]. Both are subsets of the ShapeNet dataset. The experiments demonstrate the superiority of our method over other state-of-the-art point cloud completion methods. Moreover, we also conduct experiments on the ShapeNet-34/21 [60] dataset to evaluate the performance of SnowflakeNet on novel shape completion. Then, we evaluate our method in other point cloud generation tasks, including point cloud auto-encoding, generation, single image reconstruction and upsampling.

4.1 Evaluation on the PCN Dataset

4.1.1 Dataset Briefs and Evaluation Metric

The PCN dataset [61] is a subset with eight categories derived from the ShapeNet dataset [83]. The incomplete shapes are generated by back-projecting complete shapes into eight different partial views. For each complete shape, 16,384 points are evenly sampled from the shape surface. To align with the ground truth shapes, we typically set $r_1 = 1$, $r_2 = 4$ and $r_3 = 8$ to generate complete point clouds with 16,384 points. We follow the same split settings as PCN [61] to fairly compare our SnowflakeNet with other methods. For evaluation, we adopt the L_1 version of Chamfer distance (CD), which follows the same practice as previous methods [61]. Although CD is widely used for evaluating the quality of point clouds, it may be insensitive to the global distribution. Therefore, we also use EMD as both the *completion loss* and the evaluation metric to verify the effectiveness of our method.

TABLE 1
Point Cloud Completion on the PCN Dataset in Terms of Per-Point L_1 Chamfer Distance $\times 10^3$ (Lower is Better)

Methods	Avg	Plane	Cab.	Car	Chair	Lamp	Couch	Table	Boat
Folding [11]	14.31	9.49	15.80	12.61	15.55	16.41	15.97	13.65	14.99
TopNet [8]	12.15	7.61	13.31	10.90	13.82	14.44	14.78	11.22	11.12
AtlasNet [62]	10.85	6.37	11.94	10.10	12.06	12.37	12.99	10.33	10.61
PCN [61]	9.64	5.50	22.70	10.63	8.70	11.00	11.34	11.68	8.59
GRNet [10]	8.83	6.45	10.37	9.45	9.41	7.96	10.51	8.44	8.04
CDN [9]	8.51	4.79	9.97	8.31	9.49	8.94	10.69	7.81	8.05
PMP-Net [6]	8.73	5.65	11.24	9.64	9.51	6.95	10.83	8.72	7.25
NSFA [12]	8.06	4.76	10.18	8.63	8.53	7.03	10.53	7.35	7.48
PoinTr [60]	8.38	4.75	10.47	8.68	9.39	7.75	10.93	7.78	7.29
PMP-Net++ [82]	7.56	4.39	9.96	8.53	8.09	6.06	9.82	7.17	6.52
Ours	7.21	4.29	9.16	8.08	7.89	6.07	9.23	6.55	6.40

4.1.2 Quantitative Comparison

Table 1 shows the results of our SnowflakeNet and other completion methods on the PCN dataset in terms of L_1 CD, from which we can find that SnowflakeNet achieves the best performance over all counterparts. In particular, compared with the result of the state-of-the-art PMP-Net++ [82], SnowflakeNet reduces the average CD by 0.35, which is 4.6% lower than the PMP-Net++’s results (7.56 in terms of average CD). Moreover, SnowflakeNet also achieves the best results on most categories in terms of CD, which proves the robust generalization ability of SnowflakeNet for completing shapes across different categories. In **Table 1**, both CDN [9] and NSFA [12] are typical point cloud completion methods that adopt a coarse-to-fine shape decoding strategy and model the generation of points as a hierarchical rooted tree. Compared with these two methods, our SnowflakeNet also adopts the same decoding strategy but achieves much better results on the PCN dataset. Therefore, the improvements should be credited to the proposed SPD layers and the skip-transformer in SnowflakeNet, which helps to generate points in local regions with a locally structured pattern.

Table 2 shows the quantitative results on the PCN dataset in terms of EMD, where SnowflakeNet also achieves the best overall performance (average EMD). In particular, by comparing with the second-ranked PoinTr [60], SnowflakeNet is able to reduce the average EMD by 0.232, which is 13.2% lower than PoinTr (1.764 in terms of average EMD). Compared with CD, the EMD is better at evaluating the global

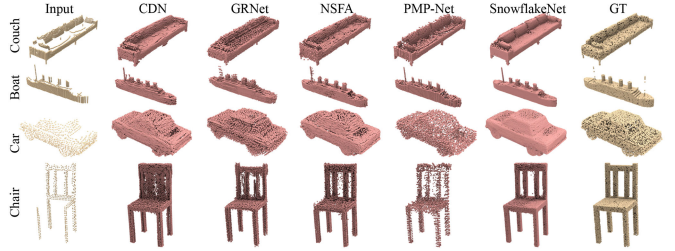


Fig. 6. Visual comparison of point cloud completion on the PCN dataset. Our SnowflakeNet can produce smoother surfaces (e.g., car) and more detailed structures (e.g., chair back) compared with the other state-of-the-art point cloud completion methods.

distribution of the completed point clouds [84], and the results in **Tables 1** and **2** can demonstrate the effectiveness of SnowflakeNet under different evaluation metrics.

4.1.3 Visual Comparison

We choose the top four point cloud completion methods from **Table 1**, and visually compare SnowflakeNet with these methods in **Fig. 6**. The visual results show that SnowflakeNet can predict the complete point clouds with a much better shape quality. For example, in the car category, the point distribution on the car’s boundary generated by SnowflakeNet is smoother and more uniform than those generated by other methods. For the chair category, SnowflakeNet can predict a more detailed and clear structure of the chair back compared with the other methods, where CDN [9] almost fails to preserve the basic structure of the chair back, while the other methods generate much noise between the columns of the chair back.

We also present a visual comparison under the EMD evaluation (see **Table 2**) in **Fig. 7**. Typically, we visually compare SnowflakeNet with two state-of-the-art methods, SpareNet [32] and PoinTr [60]. The completion results show that under the guidance of EMD loss, SnowflakeNet can produce point clouds with better visual quality that tend to maintain a consistent point distribution across the entire shape.

4.2 Evaluation on the Completion3D Dataset

4.2.1 Dataset Briefs and Evaluation Metric

The Completion3D dataset contains 30,958 models from 8 categories, of which both the partial and ground truth point clouds have 2,048 points, here we set $r_1 = 1$, $r_2 = 2$ and $r_3 = 2$ to generate complete point clouds with 2,048 points. We follow the same train/validate/testing split of Completion3D to have a fair comparison with the other methods, where the training set contains 28,974 models, the validation and testing sets contain 800 and 1,184 models, respectively. For evaluation, we adopt the L_2 version of the Chamfer distance on testing set to align with previous studies.

4.2.2 Quantitative Comparison

In **Table 3**, we show the quantitative results of our SnowflakeNet and those of the other methods on the Completion3D dataset. All results are cited from the online public leaderboard of Completion3D.¹ From **Table 3**, we can find that our

1. <https://completion3d.stanford.edu/results>

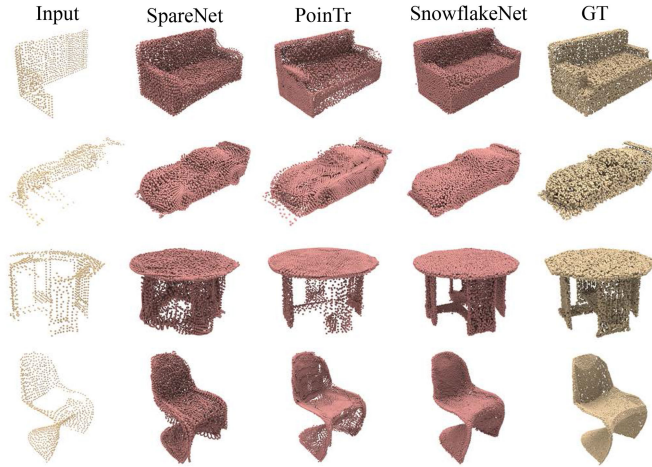


Fig. 7. Visual comparison of point cloud completion on the PCN dataset. Following the settings of MSN [13] and SpareNet [32], SnowflakeNet is trained with EMD.

SnowflakeNet achieves the best results over all methods listed on the leaderboard. In particular, compared with the latest point cloud completion methods, such as VE-PCN [25], SnowflakeNet can reduce the average CD by 0.50, which is 6.1% lower than that of the VE-PCN (8.10 in terms of average CD). Meanwhile, SnowflakeNet also outperforms the other methods in multiple categories in terms of per-category CD. Especially in the table category, SnowflakeNet reduces the per-category CD by 1.42 compared with the second-ranked result of VE-PCN. Compared with the PCN dataset, the point clouds in the Completion3D dataset have fewer points, which are easier to generate. Therefore, a coarse-to-fine decoding strategy may have fewer advantages over the other methods. Despite this, our SnowflakeNet achieves superior performance over the folding-based methods such as SA-Net [5], and our method is also the best among the coarse-to-fine methods including TopNet [8] and GRNet [10]. Overall, the results on the Completion3D dataset demonstrate the capability of SnowflakeNet to predict high-quality complete shapes using sparse point clouds.

4.2.3 Visual Comparison

Similar to the practice in the PCN dataset, we also visually compare SnowflakeNet with the top four methods in

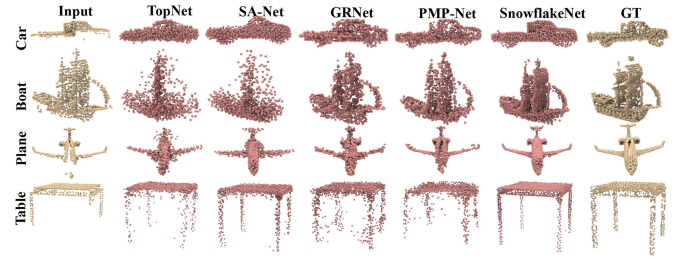


Fig. 8. Visual comparison of point cloud completion on the Completion3D dataset. Our SnowflakeNet can produce smoother surfaces (e.g., car and table) and more detailed structures compared with the other state-of-the-art point cloud completion methods.

Table 3. The visual comparison in Fig. 8 demonstrates that our SnowflakeNet also achieves much better visual results than the other counterparts on a sparse point cloud completion task. Especially, in the plane category, SnowflakeNet predicts the complete plane which is almost the same as the ground truth, while the other methods fail to reveal the complete plane in detail. The same conclusion can also be drawn from the observation of the car category. In the table and boat categories, SnowflakeNet produces more detailed structures compared with the other methods, e.g., the sails of the boat and the legs of the table.

4.3 Evaluation on the ShapeNet-34/21 Dataset

4.3.1 Dataset Briefs and Evaluation Metric

The ShapeNet-34/21 dataset [60] is derived from the original ShapeNet [83] dataset, where 34 observed shape categories are used for training, and the other 21 unseen categories are used for novel shape completion. The 34 categories of observed objects contain 50,165 objects, where those of the train/test split are 46,765 and 3,400 respectively. The unseen 21 categories contain 2,305 objects. To obtain a fair comparison, we follow the same practice of PoinTr [60] to sample 2,048 points from the object as input and 8,192 points as the ground truth, and the partial point clouds are generated online by removing the furthest n (2,048 to 6,144) points from a randomly selected viewpoint. To produce complete point clouds with 8,192 points, we set the upsampling factors to $r_1 = 1, r_2 = 4$ and $r_3 = 4$ to keep the output point number the same as other counterparts.

TABLE 3
Point Cloud Completion on the Completion3D in Terms of Per-Point L_2 Chamfer Distance $\times 10^4$ (Lower is Better)

Methods	Avg	Plane	Cab.	Car	Chair	Lamp	Couch	Table	Boat
FoldingNet [11]	19.07	12.83	23.01	14.88	25.69	21.79	21.31	20.71	11.51
PCN [61]	18.22	9.79	22.70	12.43	25.14	22.72	20.26	20.27	11.73
PointSetVoting [85]	18.18	6.88	21.18	15.78	22.54	18.78	28.39	19.96	11.16
AtlasNet [62]	17.77	10.36	23.40	13.40	24.16	20.24	20.82	17.52	11.62
SoftPoolNet [86]	16.15	5.81	24.53	11.35	23.63	18.54	20.34	16.89	7.14
TopNet [8]	14.25	7.32	18.77	12.88	19.82	14.60	16.29	14.89	8.82
SA-Net [5]	11.22	5.27	14.45	7.78	13.67	13.53	14.22	11.75	8.84
GRNet [10]	10.64	6.13	16.90	8.27	12.23	10.22	14.93	10.08	5.86
PMP-Net [6]	9.23	3.99	14.70	8.55	10.21	9.27	12.43	8.51	5.77
VRCNet [58]	8.12	3.94	10.93	6.44	9.32	8.32	11.35	8.60	5.78
VE-PCN [25]	8.10	3.83	12.74	7.86	8.66	7.24	11.47	7.88	4.75
Ours	7.60	3.48	11.09	6.90	8.75	8.42	10.15	6.46	5.32

TABLE 4
Point Cloud Completion on the ShapeNet-34/21 Dataset in Terms of the L_2 Chamfer Distance $\times 10^4$ and F-Score@1% Metric

	34 seen categories					21 unseen categories				
	CD-S (↓)	CD-M (↓)	CD-H (↓)	CD-Avg (↓)	F1 (↑)	CD-S (↓)	CD-M (↓)	CD-H (↓)	CD-Avg (↓)	F1 (↑)
Folding [11]	18.6	18.1	33.8	23.5	0.139	27.6	27.4	53.6	36.2	0.095
PCN [61]	18.7	18.1	29.7	22.2	0.154	31.7	30.8	52.9	38.5	0.101
TopNet [8]	17.7	16.1	35.4	23.1	0.171	26.2	24.3	54.4	35.0	0.121
PFNet [19]	31.6	31.9	77.1	46.8	0.347	52.9	58.7	133.3	81.6	0.322
GRNet [10]	12.6	13.9	25.7	17.4	0.251	18.5	22.5	48.7	29.9	0.216
PoinTr [60]	7.6	10.5	18.8	12.3	0.421	10.4	16.7	34.4	20.5	0.384
Ours	5.1	7.1	12.1	8.1	0.414	7.6	12.3	25.5	15.1	0.372

The CD-S, CD-M, and CD-H denote the CD results under the three difficulty levels of Simple, Moderate, and Hard.

During the evaluation, L_2 CD and F-Score [60], [87] are adopted as the evaluation metrics, where CD can evaluate the similarity between the completion results and the ground truth, and F-Score serves to evaluate the accuracy and completeness of the completed point clouds [28]. According to the removed point number n , the completion performance is evaluated under the following different difficulty degrees: *Simple* ($n = 2,048$), *Moderate* ($n = 4,096$) and *Hard* ($n = 6,144$). For each model, 8 fixed viewpoints are set to generate input point clouds. Similar to PoinTr, we present the completion results under different difficulty degrees and the averaged results.

4.3.2 Quantitative Comparison

Table 4 shows the quantitative comparison between SnowflakeNet and the other counterparts on the ShapeNet-34/21 dataset. The results in Table 4 demonstrate that our method outperforms all the other counterparts in terms of CD on the three difficulty levels, which indicates that SnowflakeNet can handle point clouds of different degrees of incompleteness, including the *Easy*, *Moderate* and *Hard* levels. Moreover, the results of the unseen categories also proved the generalization ability of SnowflakeNet on novel shape completion. Particularly, compared with PoinTr [60], SnowflakeNet reduces the CD-Avg of unseen categories by 5.4, which is 26.3% lower than that of PoinTr. Meanwhile,

SnowflakeNet also achieves competitive results in terms of F1 score, which is very close to that of PoinTr and significantly better than those of the other methods.

4.3.3 Visual Comparison

In Fig. 9, we show the visual comparison of novel shape completion, where the objects are from unseen categories during training. The completion results in Fig. 9 show that SnowflakeNet can reveal the underlying complete shapes while maintaining a visually uniform point distribution, which can be found in the bowl and the copy machine instances.

4.4 Extension to Real-World Scenarios

To evaluate the generalization ability of SnowflakeNet on real-world scenarios, we conduct experiments on the KITTI benchmark [61], [88] and the ScanNet [89] chairs.

4.4.1 Extension to the KITTI Benchmark

We test the performance of SnowflakeNet on the KITTI benchmark. Following the same practice of [60], we finetune our trained model on ShapeNet cars [83] and evaluate the performance on the KITTI benchmark. The quantitative comparison with state-of-the-art methods is shown in Table 5, where fidelity and minimal matching distance (MMD) [61] are adopted as the evaluation metrics. The visual comparison is shown in Fig. 10.

4.4.2 Extension to ScanNet Chairs

To further evaluate the performance of sparse point cloud completion in the real-world scenario, we use the pre-trained model of SnowflakeNet on the Completion3D dataset and evaluate its performance on the chair instances in the ScanNet dataset without fine-tuning. We compare SnowflakeNet with GRNet [10], VRCNet [58], VE-PCN [25], and PMP-Net++[82] and use their pre-trained models for

TABLE 5
Quantitative Comparison on the KITTI Benchmark in Terms of Fidelity and MMD Metrics

	PFNet [19]	CRN [9]	GRNet [10]	PoinTr [60]	Ours
Fidelity	1.137	1.023	0.816	0.000	0.034
MMD	0.792	0.872	0.568	0.526	0.407

Fig. 9. Visual comparison of objects from novel categories in the ShapeNet-34/21 [60] dataset.

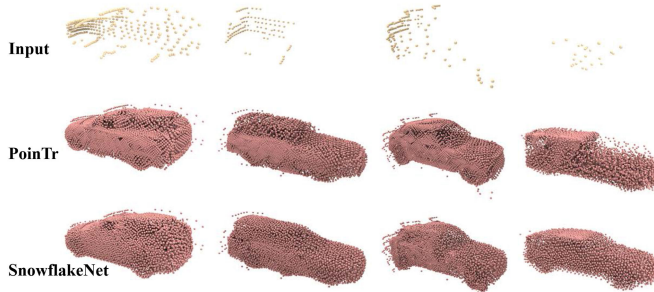


Fig. 10. Visual comparison on the KITTI benchmark.

testing. The quantitative comparison is shown in Table 6 and the visual comparison is shown in Fig. 11.

4.5 Ablation Studies

We justify the effectiveness of each part of SnowflakeNet. For convenience, we conduct ablation studies on the four categories of the Completion3D dataset. By default, all the experimental settings remain the same as in Section 4.2.

4.5.1 Effect of the Skip-Transformer

To evaluate the effectiveness of skip-transformer used in SnowflakeNet, we develop three network variations as follows. (1) The *Self-att* variation replaces the transformer mechanism in skip-transformer with the self-attention mechanism, where the input is the point features of the current layer. (2) The *No-att* variation removes the transformer mechanism from skip-transformer, where the features from the previous layer of SPD are directly added to the features of the current SPD layer. (3) The *No-connect* variation removes the whole skip-transformer from the SPD layers, and thus, no feature connection is established between the SPD layers. The experimental results are shown in Table 7. In addition, we denote the original version of SnowflakeNet as *Full* for a clear comparison with the performance of each network variation. From Table 7, we can find that the Full model achieves the best performance among all compared network variations. The comparison between the No-connect model and the Full model verifies the advantage of the skip-transformer between SPD layers, and the comparison between the No-att model and the Full model further proves the effectiveness of transformer mechanism to learn shape contexts in local regions. Moreover, the comparison between the Self-att model and the No-att model shows that the attention-based mechanism can also contribute to the completion performance.

4.5.2 Effect of Each Part in SnowflakeNet

To evaluate the effectiveness of each part in SnowflakeNet, we define four different network variations as follows. (1)



Fig. 11. Visual comparison of the chairs in the ScanNet dataset.

The *Folding-expansion* variation replaces the point-wise splitting operation with the folding-based feature expansion method [11], where the features are duplicated several times and concatenated with a 2-dimensional codeword, in order to increase the number of point features. (2) The $E_{PCN}+SPD$ variation employs the PCN encoder and our SnowflakeNet decoder. (3) The *w/o preservation loss* variation removes the partial matching loss. (4) The *PCN-baseline* is the performance of the original PCN method [61], which is trained and evaluated under the same settings as our ablation study. In Table 8, we report the results of the four network variations along with the default network denoted as *Full*. By comparing $E_{PCN}+SPD$ with PCN-baseline, we can find that our SPD with skip-transformer-based decoder can potentially be applied to other simple encoders, and achieves significant improvement. By comparing the Folding-expansion with the Full model, the better performance of the Full model proves the advantage of point-wise splitting operation over the folding-based feature expansion methods. By comparing the w/o preservation loss model with the Full model, we find that the preservation loss can slightly improve the average performance of SnowflakeNet, but has different effects on different categories.

4.5.3 The Effect of the Splitting Strategy

SPD is flexible in increasing the point number. When $r_i = 1$ (r_i is the upsampling factor of the i th SPD), it serves to

TABLE 6
Quantitative Comparison on ScanNet Chairs
in Terms of Fidelity and MMD

	GRNet [10]	VRCNet [58]	VE-PCN [25]	PMP-Net+ +[82]	Ours
Fidelity	0.36	1.53	0.10	0.82	0.12
MMD	6.62	10.44	11.32	6.22	6.29

TABLE 7
Effect of the Skip-Transformer

Methods	avg.	Couch	Chair	Car	Lamp
Self-att	8.89	6.04	10.9	9.42	9.12
No-att	9.30	6.15	11.2	10.4	9.38
No-connect	9.39	6.17	11.3	10.5	9.51
Full	8.48	5.89	10.6	9.32	8.12

TABLE 8
Effect of Each Part in SnowflakeNet

Methods	avg.	Couch	Chair	Car	Lamp
Folding-expansion	8.80	8.40	10.80	5.83	10.10
E _{PCN} +SPD	8.93	9.06	11.30	6.14	9.23
w/o preservation loss	8.50	8.72	10.6	5.78	8.9
PCN-baseline	13.30	11.50	17.00	6.55	18.20
Full	8.48	8.12	10.6	5.89	9.32

move the point from the previous step to a better position; when $r_i > 0$, it splits a point by a factor of r_i . In this section, we analyze the influence of different point splitting strategies on the performance of SnowflakeNet, and the other experimental settings are the same as those in the ablation study. As shown in Table 9, we additionally test three different splitting strategies. The one-step strategy adopts a single SPD (upsampling factor is 4) to split \mathcal{P}_0 (512 points) to \mathcal{P}_1 (2048 points). The two-step strategy adopts two SPDs (upsampling factors are both equal to 2) and produces three point clouds \mathcal{P}_0 , \mathcal{P}_1 , and \mathcal{P}_2 with a size of 512×3 , 1024×3 , and 2048×3 , respectively. For the three-step strategy (three SPDs of upsampling factor 2), we particularly set $N_c = N_0 = 256$ (see Section 3.1) so that it outputs 4 point clouds of the sizes 256×3 , 512×3 , 1024×3 , and 2048×3 . Note that the baseline is two-step splitting with an additional SPD (upsampling factor equals 1), which serves to rearrange the initial point positions. By comparing the one-step strategy with the other strategies, we can find that multiple steps of splitting boost the performance of SnowflakeNet significantly (in terms of average CD), this should credit to the collaboration between SPDs. By comparing two-step strategy with three-step strategy, we can find that the two-step splitting suffices for generating a sparse point cloud with 2048 points (not necessarily for a dense one with more points), and extra SPDs may not improve the performance but will increase the computational burden. By comparing the two-step strategy with the baseline, we can find that the additional SPD that adjusts the initial point positions can facilitate the point splitting process.

4.5.4 Effect of Neighbor Number k

As mentioned in Section 3.3, the skip-transformer aggregates local geometric pattern among the k nearest neighbors. Therefore, Table 10 shows the effect of k , which is denoted as *Full*. Additionally, since *Self-att* variation (see Table 7) also adopts the k -NN strategy to conduct self-attention, we also explore its performance. The results in Table 10 indicate that under different neighbor numbers k , the *Full* model outperforms the *Self-att* variation. Moreover, a small

TABLE 9
Effect of the Splitting Strategy

Splitting strategy	avg.	Couch	Chair	Car	Lamp
one-step	9.53	6.03	11.0	9.94	9.26
two-steps	8.64	6.00	10.3	9.62	8.66
baseline	8.48	5.89	10.6	9.32	8.12
three-steps	8.66	6.04	10.0	9.53	9.02

TABLE 10
Effect of k -NN

k	4	8	16	32	64
Self-att	8.83	8.71	8.89	8.64	8.61
Full	8.69	8.51	8.48	8.37	8.38

k (4, 8, and 16) cannot help to improve the performance of *Self-att*. In contrast, the performance of the *Full* model can steadily improve as the k increases from 4 to 32, which further proves the necessity and effectiveness of skip-transformer. Furthermore, as k becomes larger, the performance of *Full* will not change dramatically, since an oversized neighborhood could introduce noise and the skip-transformer cannot focus on the local context. In our paper, we set k to 16 to balance the trade-off between performance and inference efficiency.

4.5.5 Robustness to Random Noise

We explored the robustness of SnowflakeNet to noise perturbation by adding Gaussian noise to the input point clouds, and the results are shown in Table 11. During training, we add zero mean Gaussian noise and change the noise degree by randomly adjusting the standard deviation, which ranges from 0 (0%) to 0.02 (denoted as 2.0% in Table 11). During the evaluation, we test the performance on five noise levels (0%, 0.5%, 1.0%, 1.5% and 2.0%). The quantitative results in Table 11 show that the random noise during training can hamper the performance on noise-free point clouds (by comparing 0% with baseline). However, training with noisy point clouds could also significantly improve the robustness to moderate noise degrees, where the network performs stably under noise perturbation levels ranging from 0.5% to 1.5%. As the noise level dramatically increases (2.0%), the quantitative performance will degrade due to the large corruption of partial inputs. We also present visual results under different noise levels in Fig. 12, from which we can find that under the 2.0% noise level, the input point cloud almost lost its underlying structure (see the car instance), but our model can still complete the overall shape and produce plausible point clouds.

4.5.6 Visualization of Point Generation Process of SPD

In Fig. 13, we visualize the point cloud generation process of SPD. We can find that the SPD layers generate points in a snowflake-like pattern. When generating the smooth plane

TABLE 11
Robustness to Random Noise

Noise levels	avg.	Couch	Chair	Car	Lamp
baseline	8.48	5.89	10.60	9.32	8.12
0%	8.81	6.04	11.05	9.05	9.09
0.5%	8.79	6.10	11.00	8.94	9.14
1.0%	8.90	6.32	10.99	9.11	9.17
1.5%	9.37	6.65	11.59	9.48	9.78
2.0%	10.56	7.29	13.21	10.72	11.04

We add noise of levels ranging from 0% to 2.0%, where 2.0% denotes zero mean Gaussian noise and the standard deviation is set to 0.02.

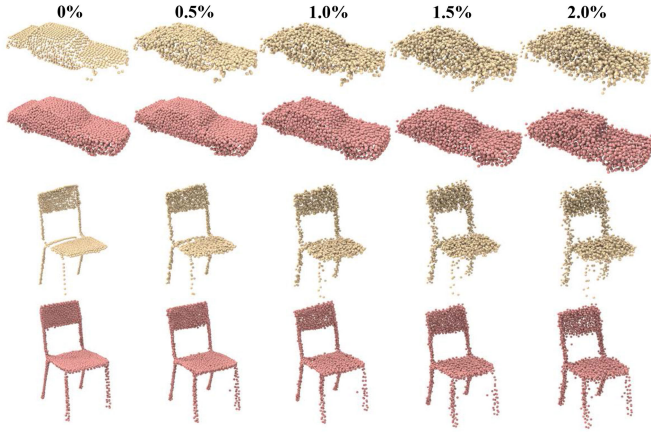


Fig. 12. Completion results under different noise levels.

(e.g., chair and lamp in Fig. 13), we can see the child points are generated around the parent points and are smoothly placed along the plane surface. However, when generating thin tubes and sharp edges, the child points can precisely capture the geometries.

4.6 Point Cloud Auto-Encoding

The task of point cloud auto-encoding aims to reconstruct a point cloud from its reduced and encoded representation. Since it heavily relies on the generation ability of the decoder, we use the decoding part of SnowflakeNet in point cloud auto-encoding to evaluate the generation ability of snowflake point deconvolution.

4.6.1 Dataset and Evaluation Metric

Dataset. To fairly evaluate the generation ability of SPD, we follow the same experimental settings of DPM [63] and conduct point cloud auto-encoding on the ShapeNet [83] dataset. The ShapeNet [83] dataset contains 51,127 shapes from 55 categories. We use the same training, testing, and evaluation split of DPM [63], where the ratios of training, testing and, validation sets are 80%, 15%, and 5%, respectively. To evaluate the generation ability under both simple and difficult settings, we conduct experiments on three categories (i.e., *car*, *airplane* and *chair*) of ShapeNet separately, and also verify the performance of SPD on the entire ShapeNet dataset.

Evaluation Metric. The commonly used Chamfer distance (CD) and Earth Mover's distance (EMD) are adopted as the evaluation metrics.

4.6.2 Network Arrangement and Training Loss

Network Arrangement. The auto-encoding task aims to evaluate the reconstruction ability of our decoder. We follow DPM and replace our feature extractor with a simple PointNet [81] encoder, so that the encoding settings are the same as those of other methods. In addition, the ground truth shapes used in auto-encoding have 2,048 points, so we use our seed generator and two stacked SPDs (each has an upsampling factor of 2) as the decoder. In the seed generator, we set N_c to 512 and take \mathcal{P}_c as the output of the seed generator, where \mathcal{P}_c and \mathcal{P}_0 are the same point cloud. This

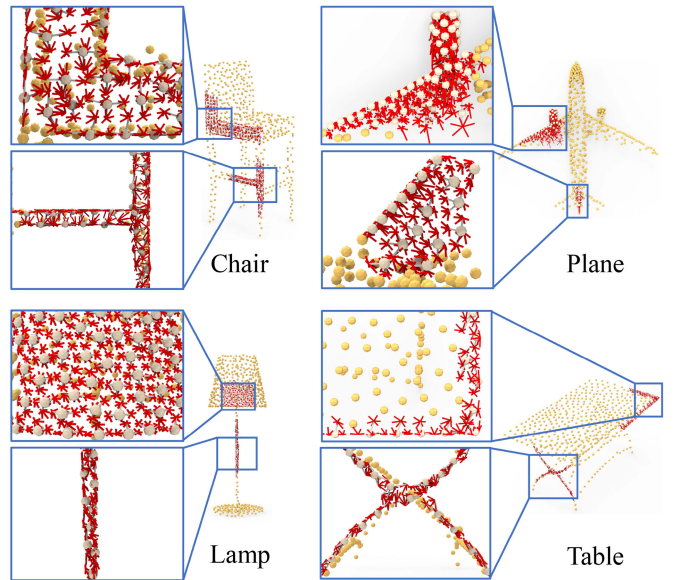


Fig. 13. Visualization of snowflake point deconvolution on different objects. For each object, we sample two patches of points and visualize two layers of point splitting together for each sampled point. The gray lines indicate the paths of the point splitting from \mathcal{P}_1 to \mathcal{P}_2 , and the red lines are splitting paths from \mathcal{P}_2 to \mathcal{P}_3 .

arrangement ensures that the generation of point cloud relies only on the latent code extracted from the encoder.

Training Loss. We use L_2 Chamfer distance (CD) in Eq. (6) and Earth Mover's distance (EMD) in Eq. (9) as our reconstruction loss, which is given as follows:

$$\mathcal{L}_{recon} = \sum_{i \in \{0, 2\}} \mathcal{L}_{CD_2}(\mathcal{P}_i, \mathcal{P}'_i) + \mathcal{L}_{EMD}(\mathcal{P}_i, \mathcal{P}'_i), \quad (12)$$

where \mathcal{P}'_i is the downsampled ground truth shape that has the same point density of \mathcal{P}_i .

4.6.3 Quantitative Comparison

The quantitative comparison is given in Table 12. Even though only two SPDs are used in the decoder, our method still achieves the best performance among the compared counterparts in terms of both L_2 CD and EMD. Especially on the entire ShapeNet dataset, SnowflakeNet reduces the average CD by 1.05, which is 20% lower than that of DPM [63] (5.25 in terms of average CD). At the same time, our method also outperforms the other methods across all categories in terms of per-category CD and EMD. Therefore, the better results on point cloud auto-encoding fully demonstrate the generation ability of the decoder of our SnowflakeNet, especially snowflake point deconvolution.

4.6.4 Visual Comparison

The qualitative comparison is shown in Fig. 14. We visually compare SnowflakeNet with the state-of-the-art generation method DPM. Fig. 14 shows that SnowflakeNet is able to generate point clouds with more detailed geometric structures, such as the handle of the cup and the motor tires. Meanwhile, the points generated by SnowflakeNet are much more uniform and tend to cover the surface of the shape evenly, which should be credited to the excellent

TABLE 12
Comparison of Point Cloud Auto-Encoding in Terms of CD and EMD on ShapeNet

Dataset	Metric	Atlas (S1) [62]	Altas (P25) [62]	PointFlow [64]	ShapeGF [73]	DPM [63]	Ours
Airplane	CD	2.00	1.80	2.42	2.10	2.19	1.51
	EMD	4.31	4.37	3.31	3.50	2.90	2.44
Car	CD	6.91	6.50	5.83	5.47	5.49	4.68
	EMD	5.67	5.41	4.39	4.49	3.94	3.35
Chair	CD	5.48	4.98	6.80	5.15	5.68	4.58
	EMD	5.56	5.28	5.01	4.78	4.15	3.67
ShapeNet	CD	5.87	5.42	7.55	5.73	5.25	4.20
	EMD	5.46	5.60	5.17	5.05	3.78	3.44

L_2 CD and EMD are multiplied by 10^4 and 10^2 , respectively.

generation ability of SPDs. In addition, we visualize the interpolation and extrapolation between latent codes in Fig. 15, where the source shapes are in yellow, and the interpolated and extrapolated shapes are in red. Fig. 15 shows that the output of SnowflakeNet is able to transit smoothly according to latent interpolation and extrapolation, even though the transition is between different categories (table and chair, the last row). Moreover, the interpolated and extrapolated shapes can still maintain a visually uniform point distribution, which shows the generation stability of our decoder.

4.7 Novel Shape Generation

In addition to point cloud auto-encoding, we also apply our network to point cloud generation to demonstrate its novel shape generation ability.

4.7.1 Dataset and Evaluation Metric

Dataset. For the task of point cloud generation, we follow DPM [63] and conduct experiments on the ShapeNet dataset. We quantitatively compare our method with several state-of-the-art generative models on the two categories (i.e., airplane and chair) in ShapeNet. The generated point clouds and the reference point clouds are normalized into a bounding box of $[-1, 1]$.

Evaluation Metric. To evaluate the generation quality of our method, we follow prior works [63], [64], [73] and

employ the coverage score (COV), the minimum matching distance (MMD), the 1-NN classifier accuracy (1-NNA), and the Jenson-Shannon divergence (JSD). The COV score measures whether the generated samples cover all the modes of the data distribution and the MMD score measures the fidelity of the generated samples. The 1-NNA measures the similarity between the distributions of the generated samples and the reference samples. If the accuracy of the 1-NN classifier is closer to 50% (random guess), and the generation quality is considered to be better. The JSD score measures the similarity between the marginal point distributions of the generated set and the reference set. Meanwhile, we adopt L_2 CD and EMD to evaluate the reconstruction quality.

4.7.2 Network Arrangement and Training Loss

Network Arrangement. The network arrangement in this section is the same as point cloud auto-encoding (Section 4.6.2).

Training Loss. To help our decoder to generate novel shapes, we employ normalizing flows [63], [90], [91] to parameterize the prior distribution $p(\mathbf{f})$, where \mathbf{f} is the latent code extracted by the encoder. The normalizing flow is essentially a stack of affine coupling layers, which provides a trainable bijection F_α that maps an isotropic Gaussian to a complex distribution [63]. The prior distribution can be computed by

$$p(\mathbf{f}) = p_{\mathbf{w}}(\mathbf{w}) \cdot \left| \det \frac{\partial F_\alpha}{\partial \mathbf{w}} \right|^{-1}, \quad (13)$$

where $\mathbf{w} = F_\alpha^{-1}(\mathbf{f})$, and $p_{\mathbf{w}}(\mathbf{w})$ is the isotropic Gaussian $\mathcal{N}(\mathbf{0}, I)$. Similar to DPM [63], we adopt PointNet [81] as the architecture for μ and Σ of the encoder $q(\mathbf{f}|\mathcal{P})$. Together



Fig. 14. Visual comparison of reconstructed point clouds between different auto-encoders.

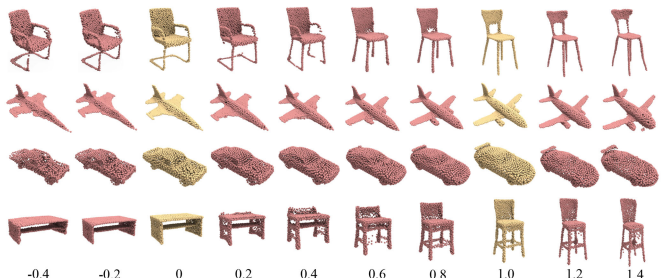


Fig. 15. Latent space interpolation and extrapolation. The interpolation step is 0.2, the source shapes are in yellow (denoted as “0” and “1.0”), and the interpolated and extrapolated shapes are in red.

TABLE 13
Comparison of Novel Point Cloud Generation Performance in Terms of L_2 CD and EMD

Shape	Model	COV(%), \uparrow		MMD(\downarrow)		1-NNA(%), \downarrow		JSD(\downarrow)
		CD	EMD	CD	EMD	CD	EMD	
Airplane	PC-GAN [70]	42.17	13.84	3.819	1.810	77.59	98.52	6.188
	GCN-GAN [71]	39.04	18.62	4.713	1.650	89.13	98.60	6.669
	TreeGAN [72]	39.37	8.40	4.323	1.953	83.86	99.67	15.646
	PointFlow [64]	44.98	44.65	3.688	1.090	66.39	69.36	1.536
	ShapeGF [73]	50.41	47.12	3.306	1.027	61.94	70.51	1.059
	DPM [63]	48.71	45.47	3.276	1.061	64.83	75.12	1.067
Chair	Ours	46.29	44.98	3.271	1.002	69.35	73.15	1.630
	PC-GAN [70]	46.23	22.14	13.436	3.104	69.67	100.00	6.649
	GCN-GAN [71]	39.84	35.09	15.354	2.213	77.86	95.80	21.708
	TreeGAN [72]	38.02	6.77	14.936	3.613	74.92	100.00	13.282
	PointFlow [64]	41.86	43.38	13.631	1.856	66.13	68.40	12.474
	ShapeGF [73]	48.53	46.71	13.175	1.785	56.17	62.69	5.996
	DPM [63]	48.94	47.52	12.276	1.784	60.11	69.06	7.797
Ours		48.83	36.91	12.742	1.830	58.85	75.08	7.579

CD is multiplied by 10^4 and EMD is multiplied by 10^2 .

with the reconstruction loss in Eq. (12), the training loss for point cloud generation is given as follows:

$$\mathcal{L}_{gen} = D_{KL}(q(\mathbf{f}|\mathcal{P})||p_{\mathbf{w}}(\mathbf{w}) \cdot \left| \det \frac{\partial F_{\alpha}}{\partial \mathbf{w}} \right|^{-1}) + \mathcal{L}_{recon}, \quad (14)$$

where D_{KL} is the KL divergence. To generate a point cloud, we first obtain the latent code \mathbf{f} by drawing $\mathbf{w} \sim \mathcal{N}(\mathbf{0}, I)$ and pass \mathbf{w} through F_{α} and then pass the latent \mathbf{f} to our decoder.

4.7.3 Quantitative and Qualitative Results

In Table 13, we quantitatively compare our methods with the following state-of-the-art generative models: DPM [63], ShapeGF [73], PointFlow [64], TreeGAN [72], GCN-GAN [71], and PC-GAN [70]. We follow the same experimental settings as DPM [63] and all the other results are cited from DPM [63]. Table 13 shows that our method is highly competitive compared to the latest generative models, such as ShapeGF [73] and DPM [63], and is significantly

better than the other methods. Moreover, we also achieve the best results on the MMD score of the airplane category, which proves the generation ability of our method. In Fig. 16, we visually present some point cloud samples generated by our method, from which we find that our method is able to generate novel shapes with good uniformity. Although the latent code is randomly sampled from Gaussian distribution, which leads uncertainty to the decoder, our method can still generate diverse novel shapes while maintaining enriched local geometric structures. Therefore, the visual generation results further demonstrate the excellent generation quality of our snowflake point deconvolution.

4.8 Single Image Reconstruction

In this section, we extend our network to the task of single image reconstruction (SVR), of which the goal is to reconstruct a point cloud from an image of the underlying object.

4.8.1 Dataset and Evaluation Metric

Dataset. For the single view reconstruction task, we employ the ShapeNet [83] dataset containing 43783 shapes from 13 categories. The dataset is split into training, testing, and validation sets by the ratios of 70%, 20%, and 10%, respectively. During training, we track the loss of our method on the validation set to determine when to stop training. The testing set is used for quantitative and qualitative comparison. The baseline methods include 3D-R2N2 [92], PSGN [68], Pixel2-Mesh [93], AtlasNet [62], OccNet [94], and the state-of-the-art methods like Pix2Vox [95], Pix2Vox++ [96], DPM [63], and 3DAtriflow [69]. For a fair comparison, we follow [69], [94] and sample 30 k points from the watertight mesh as the ground truth.

Evaluation Metric. We adopt the L_1 Chamfer distance (CD) to evaluate the generation quality among all counterparts. In our experiment, we set the output point density of all methods to 2,048. The output points of voxel-based (Pix2Vox [96]) and mesh-based (Pixel2Mesh [93] and OccNet [94])

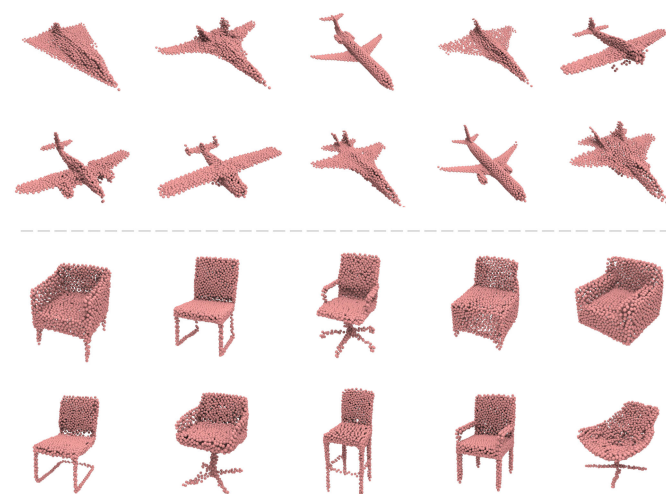


Fig. 16. Examples of novel point clouds generated by our model.

TABLE 14
Single Image Reconstruction on the ShapeNet Dataset in Terms of Per-Point L_1 Chamfer Distance $\times 10^2$ (Lower is Better)

Methods	Average	Plane	Bench	Cabinet	Car	Chair	Display	Lamp	Loud.	Rifle	Sofa	Table	Tele.	Vessel
3DR2N2 [92]	5.41	4.94	4.80	4.25	4.73	5.75	5.85	10.64	5.96	4.02	4.72	5.29	4.37	5.07
PSGN [68]	4.07	2.78	3.73	4.12	3.27	4.68	4.74	5.60	5.62	2.53	4.44	3.81	3.81	3.84
Pixel2mesh [93]	5.27	5.36	5.14	4.85	4.69	5.77	5.28	6.87	6.17	4.21	5.34	5.13	4.22	5.48
AtlasNet [62]	3.59	2.60	3.20	3.66	3.07	4.09	4.16	4.98	4.91	2.20	3.80	3.36	3.20	3.40
OccNet [94]	4.15	3.19	3.31	3.54	3.69	4.08	4.84	7.55	5.47	2.97	3.97	3.74	3.16	4.43
Pix2Vox [95]	4.28	3.48	4.47	4.39	3.56	4.04	4.47	5.66	5.10	3.80	4.37	4.29	3.84	4.14
Pix2Vox++ [96]	4.17	3.65	4.40	3.99	3.48	3.97	4.40	5.63	4.84	3.78	4.12	4.01	3.68	4.28
DPM [63]	3.76	2.64	3.56	3.46	3.23	4.15	4.35	5.18	5.14	2.41	4.15	3.71	3.42	3.52
3DAttrFlow [69]	3.02	2.11	2.71	2.66	2.50	3.33	3.60	4.55	4.16	1.94	3.24	2.85	2.66	2.96
Ours	2.86	1.99	2.54	2.52	2.44	3.13	3.37	4.34	3.98	1.84	3.09	2.71	2.45	2.80

methods are sampled on their generated mesh, and the sampling strategy is the same as [94].

4.8.2 Network Arrangement and Training Loss

Network Arrangement. The network framework of SVR consists of an encoder and a decoder. We use ResNet [97] (ResNet-18) as the encoder to align with the other baseline methods, and the dimension of the latent code is transformed to 128 by a *linear* layer. For our decoder, the arrangement is the same as auto-encoding (Section 4.6.2).

Training Loss. We use the Chamfer- L_1 distance (CD) as the training loss for single image reconstruction, which is given as

$$\mathcal{L}_{\text{SVR}} = \sum_{i \in \{0,2\}} \mathcal{L}_{\text{CD}_i}(\mathcal{P}_i, \mathcal{P}_i^i). \quad (15)$$

4.8.3 Quantitative Comparison

In Table 14, we quantitatively compare our method with the baseline methods listed in Section 4.8.1. The quantitative results in Table 14 demonstrate that our method has the best reconstruction performance among all compared methods. Moreover, our method achieves the best per-category CD across all shape categories, which fully demonstrates the generalization ability of our method.

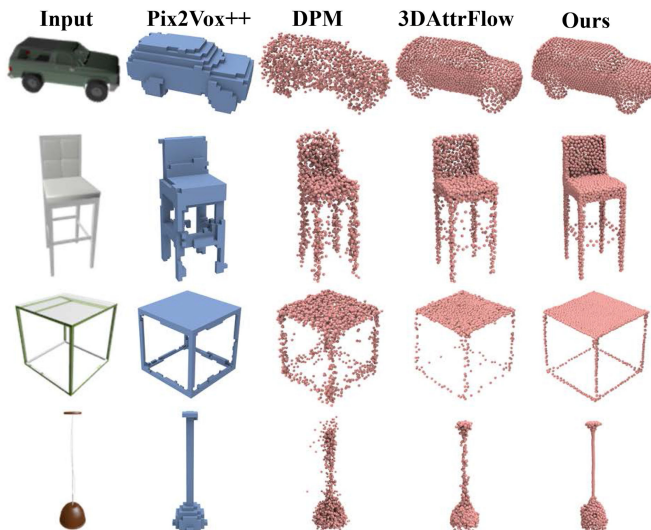


Fig. 17. Visual comparison of single image reconstruction. Voxels are in blue, and point clouds are in red.

4.8.4 Visual Comparison

We visually compare the reconstruction results in Fig. 17, which illustrates the best reconstruction quality of our method among all baseline methods. Limited to voxel resolution, the reconstruction results of Pix2Vol++[96] can accurately reconstruct the overall shape but fail to reveal detailed geometries. DPM [63] produces too much noise and requires additional denoising in post-processing steps. Compared with 3DAttrFlow [69], our method is able to reconstruct the underlying object while recovering smooth surfaces, and the SPD enables our decoder to produce shapes with less noise and smoother surfaces.

4.9 Point Cloud Upsampling

Given a sparse, noisy, and non-uniform point cloud, the task of point cloud upsampling requires upsampling and generating a dense and uniform point cloud. Because it is also a generation problem, we extend snowflake point deconvolution (SPD) to point cloud upsampling in this section.

4.9.1 Dataset and Evaluation Metric

Dataset. To compare the upsampling quality of SPD with state-of-the-art methods, we use the benchmark dataset provided by PU-GAN [55] with 120 training and 27 testing objects. Each training object is cropped into 200 overlapped patches, and there are a total of 24,000 training surface patches. Each surface patch has 1,024 points. During training, we randomly sample 256 points as input. For testing objects, we follow [55] and use Poisson disk sampling to sample 8192 points as the ground truth shape, and 2,048 points are further sampled as input. Since the performance of point cloud upsampling is highly sensitive to the quality

TABLE 15
Quantitative Comparison on the Point Cloud Upsampling Task in Terms of CD $\times 10^3$ and HD $\times 10^3$

Methods	Size	FPS		RS	
		CD	HD	CD	HD
PU-Net [14]	10.1 M	0.473	4.680	0.532	5.441
PU-GAN [55]	9.57 M	0.246	3.011	0.269	4.687
Dis-PU [67]	13.2 M	0.210	2.771	0.278	4.289
Ours	1.37 M	0.199	2.701	0.270	3.787

FPS stands for farthest point sampling, and RS denotes random sampling.

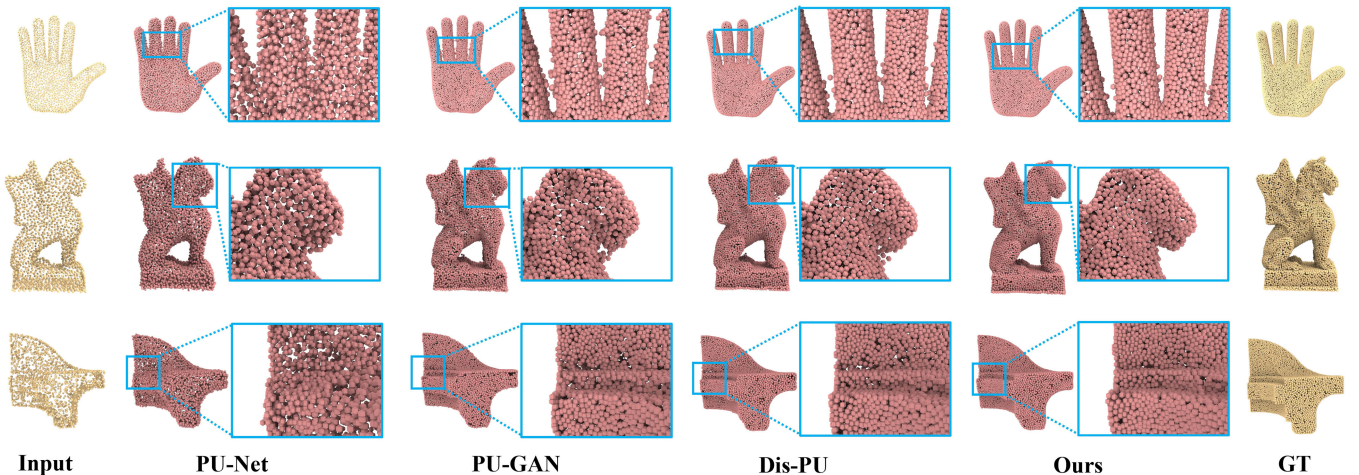


Fig. 18. Visual comparison of point cloud upsampling.

of input point clouds, we get the inputs under two settings: farthest point sampling (FPS) [81] and random sampling. To mitigate the instability brought by random sampling, we repeat the test under random sampling five times and take the average scores as the final results.

Evaluation Metric. We use the L_2 Chamfer distance (CD) and the Hausdorff distance (HD) [98] as the evaluation metric for a fair comparison with other methods.

4.9.2 Network Arrangement and Training Loss

Network Arrangement. For the task of point cloud upsampling, four stacked SPDs are used to upsample the sparse point cloud into a dense one. The upsampling factors r_1, r_2, r_3 , and r_4 of the four SPDs are 1, 2, 2, 1, respectively. Because point cloud upsampling requires the output point cloud to be uniform, we add another SPD (of which $r_4 = 1$) to refine the upsampled point cloud.

Training Loss. We use only the L_2 Chamfer distance (CD) to train our network, and the training loss is given as follows:

$$\mathcal{L}_{upsampling} = \sum_{i \in \{1,3,4\}} \mathcal{L}_{CD_2}(\mathcal{P}_i, \mathcal{P}'_i), \quad (16)$$

where \mathcal{P}'_i is the downsampled ground truth shape that has the same point density as \mathcal{P}_i .

4.9.3 Quantitative Comparison

In Table 15, we quantitatively compare our method with the following state-of-the-art point cloud upsampling methods: PU-Net [14], PU-GAN [55], and Dis-PU [67]. FPS stands for farthest point sampling, and RS denotes random sampling. We use the pre-trained models provided by these methods for testing on the same test set. From Table 15, we can find that our method achieves the best performance in terms of both L_2 CD and HD under the FPS setting. Even though our method is not trained with repulsion loss [14] or uniform loss [55], our method can recover the underlying surface while maintaining good point uniformity. Meanwhile, under the RS setting, the CD scores of PU-GAN, Dis-PU, and SPD (Ours) are highly close to each other, and we achieve a much better result in terms of HD. Moreover, by comparing the model size with the other methods in terms of parameter number, we find that the model size of our

method is significantly smaller than those of the others, which further proves the efficiency of snowflake point deconvolution.

4.9.4 Visual Comparison

In Fig. 18, we visually compare our method with the state-of-the-art methods listed in Table 15. From Fig. 18, we can find that our method can produce the most similar visual results to the ground truth shape. Whether the ground truth shape has complex tiny local structures (the second shape) or simple flat regions (the third shape), our method can preserve a uniform point distribution.

5 CONCLUSION, LIMITATION AND FUTURE WORK

In this paper, we propose a novel neural network for point cloud completion, named SnowflakeNet. SnowflakeNet models the generation of complete point clouds as the snowflake-like growth of points in 3D space using multiple layers of snowflake point deconvolution (SPD). By further introducing a skip-transformer in SPD, SnowflakeNet learns to generate locally compact and structured point clouds with highly detailed geometries. We conduct comprehensive experiments on sparse (Completion3D) and dense (PCN) point cloud completion datasets, which shows the superior performance of our method over the current SOTA point cloud completion methods. We further extend SPD to more point cloud generation tasks, such as point cloud auto-encoding, novel point cloud generation, single image reconstruction, and upsampling. The generation ability of Snowflake Point Deconvolution is fully demonstrated by both quantitative and qualitative experimental results.

The main limitation of SnowflakeNet is that the skip-transformer in SPD merely aggregates information from the k -nearest neighbors (k -NN) of each point. While the k -NN strategy enables the SPD to focus on local structure, it also disenables the SPD to capture the long-range shape context. Therefore, when the input point cloud contains too much noise, SPD is unable to arrange point splitting properly. In our opinion, a potential and promising future work to address this problem is to further explore the local and global feature fusion in SPD, so that SPD can adapt well to more complex shape contexts.

Another limitation is that SPD generates the same number of child points for all seed points, despite different numbers of points being needed to represent different parts of the shape. For example, it requires more points to represent the lampshade than the lamppost. It would be ideal if SPD can adaptively split seed points based on the complexity of local shape contexts; this may require significant changes to the network.

ACKNOWLEDGMENTS

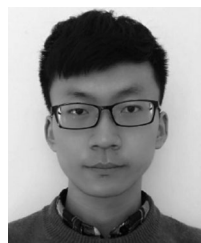
Source code is available at <https://github.com/AllenXiangX/SnowflakeNet>. Peng Xiang and Xin Wen contributed equally to this work.

REFERENCES

- [1] Z. Han, C. Chen, Y.-S. Liu, and M. Zwicker, "ShapeCaptioner: Generative caption network for 3D shapes by learning a mapping from parts detected in multiple views to sentences," in *Proc. 28th ACM Int. Conf. Multimedia*, 2020, pp. 1018–1027.
- [2] Z. Han, M. Shang, Y.-S. Liu, and M. Zwicker, "View inter-prediction GAN: Unsupervised representation learning for 3D shapes by learning global shape memories to support local view predictions," in *Proc. 33rd AAAI Conf. Artif. Intell.*, 2019, pp. 8376–8384.
- [3] Z. Han, M. Shang, X. Wang, Y.-S. Liu, and M. Zwicker, "Y2Seq2Seq: Cross-modal representation learning for 3D shape and text by joint reconstruction and prediction of view and word sequences," in *Proc. 33th AAAI Conf. Artif. Intell.*, 2019, pp. 126–133.
- [4] Z. Han et al., "BoSCC: Bag of spatial context correlations for spatially enhanced 3D shape representation," *IEEE Trans. Image Process.*, vol. 26, no. 8, pp. 3707–3720, Aug. 2017.
- [5] X. Wen, T. Li, Z. Han, and Y.-S. Liu, "Point cloud completion by skip-attention network with hierarchical folding," in *Proc. IEEE Conf. Comput. Vis. Pattern Recognit.*, 2020, pp. 1939–1948.
- [6] X. Wen et al., "PMP-Net: Point cloud completion by learning multi-step point moving paths," in *Proc. IEEE Conf. Comput. Vis. Pattern Recognit.*, 2021, pp. 7439–7448.
- [7] X. Wen, Z. Han, Y.-P. Cao, P. Wan, W. Zheng, and Y.-S. Liu, "Cycle4Completion: Unpaired point cloud completion using cycle transformation with missing region coding," in *Proc. IEEE Conf. Comput. Vis. Pattern Recognit.*, 2021, pp. 13075–13084.
- [8] L. P. Tchapmi, V. Kosaraju, H. Rezatofighi, I. Reid, and S. Savarese, "TopNet: Structural point cloud decoder," in *Proc. IEEE Conf. Comput. Vis. Pattern Recognit.*, 2019, pp. 383–392.
- [9] X. Wang, M. H. Ang Jr, and G. H. Lee, "Cascaded refinement network for point cloud completion," in *Proc. IEEE Conf. Comput. Vis. Pattern Recognit.*, 2020, pp. 790–799.
- [10] H. Xie, H. Yao, S. Zhou, J. Mao, S. Zhang, and W. Sun, "GRNet: Gridding residual network for dense point cloud completion," in *Proc. Eur. Conf. Comput. Vis.*, 2020, pp. 365–381.
- [11] Y. Yang, C. Feng, Y. Shen, and D. Tian, "FoldingNet: Point cloud auto-encoder via deep grid deformation," in *Proc. IEEE Conf. Comput. Vis. Pattern Recognit.*, 2018, pp. 206–215.
- [12] W. Zhang, Q. Yan, and C. Xiao, "Detail preserved point cloud completion via separated feature aggregation," in *Proc. Eur. Conf. Comput. Vis.*, 2020, pp. 512–528.
- [13] M. Liu, L. Sheng, S. Yang, J. Shao, and S.-M. Hu, "Morphing and sampling network for dense point cloud completion," in *Proc. AAAI Conf. Artif. Intell.*, 2020, pp. 11596–11603.
- [14] Y. Lequan, L. Xianzhi, F. Chi-Wing, C.-O. Daniel, and H. Pheng Ann, "PU-Net: Point cloud upsampling network," in *Proc. IEEE Int. Conf. Comput. Vis.*, 2018, pp. 2790–2799.
- [15] M. Sung, V. G. Kim, R. Angst, and L. Guibas, "Data-driven structural priors for shape completion," *ACM Trans. Graph.*, vol. 34, no. 6, 2015, Art. no. 175.
- [16] M. Berger et al., "State of the art in surface reconstruction from point clouds," in *Proc. Eurographics*, 2014, pp. 161–185.
- [17] D. Thanh Nguyen, B.-S. Hua, K. Tran, Q.-H. Pham, and S.-K. Yeung, "A field model for repairing 3D shapes," in *Proc. IEEE Conf. Comput. Vis. Pattern Recognit.*, 2016, pp. 5676–5684.
- [18] W. Hu, Z. Fu, and Z. Guo, "Local frequency interpretation and non-local self-similarity on graph for point cloud inpainting," *IEEE Trans. Image Process.*, vol. 28, no. 8, pp. 4087–4100, Aug. 2019.
- [19] Z. Huang, Y. Yu, J. Xu, F. Ni, and X. Le, "PF-Net: Point fractal network for 3D point cloud completion," in *Proc. IEEE Conf. Comput. Vis. Pattern Recognit.*, 2020, pp. 7662–7670.
- [20] X. Chen, B. Chen, and N. J. Mitra, "Unpaired point cloud completion on real scans using adversarial training," in *Proc. Int. Conf. Learn. Representations*, 2020.
- [21] J. Gu et al., "Weakly-supervised 3D shape completion in the wild," in *Proc. Eur. Conf. Comput. Vis.*, 2020, pp. 283–299.
- [22] Y. Nie et al., "Skeleton-bridged point completion: From global inference to local adjustment," in *Proc. Adv. Neural Inf. Process. Syst.*, 2020, pp. 16119–16130.
- [23] T. Hu, Z. Han, and M. Zwicker, "3D shape completion with multi-view consistent inference," in *Proc. AAAI Conf. Artif. Intell.*, 2020, pp. 10997–11004.
- [24] T. Hu, Z. Han, A. Shrivastava, and M. Zwicker, "Render4Completion: Synthesizing multi-view depth maps for 3D shape completion," in *Proc. IEEE/CVF Int. Conf. Comput. Vis.*, 2019, pp. 4114–4122.
- [25] X. Wang, M. H. Ang, and G. H. Lee, "Voxel-based network for shape completion by leveraging edge generation," in *Proc. IEEE/CVF Int. Conf. Comput. Vis.*, 2021, pp. 13189–13198.
- [26] A. Alliegro, D. Valsesia, G. Fracastoro, E. Magli, and T. Tommasi, "Denoise and contrast for category agnostic shape completion," in *Proc. IEEE/CVF Conf. Comput. Vis. Pattern Recognit.*, 2021, pp. 4629–4638.
- [27] T. Huang et al., "RFNNet: Recurrent forward network for dense point cloud completion," in *Proc. IEEE/CVF Int. Conf. Comput. Vis.*, 2021, pp. 12508–12517.
- [28] J. Zhang et al., "Unsupervised 3D shape completion through GAN inversion," in *Proc. IEEE/CVF Conf. Comput. Vis. Pattern Recognit.*, 2021, pp. 1768–1777.
- [29] B. Gong, Y. Nie, Y. Lin, X. Han, and Y. Yu, "ME-PCN: Point completion conditioned on mask emptiness," in *Proc. IEEE/CVF Int. Conf. Comput. Vis.*, 2021, pp. 12488–12497.
- [30] L. Zhou, Y. Du, and J. Wu, "3D shape generation and completion through point-voxel diffusion," in *Proc. IEEE/CVF Int. Conf. Comput. Vis.*, 2021, pp. 5826–5835.
- [31] X. Zhang et al., "View-guided point cloud completion," in *Proc. IEEE/CVF Conf. Comput. Vis. Pattern Recognit.*, 2021, pp. 15890–15899.
- [32] C. Xie, C. Wang, B. Zhang, H. Yang, D. Chen, and F. Wen, "Style-based point generator with adversarial rendering for point cloud completion," in *Proc. IEEE/CVF Conf. Comput. Vis. Pattern Recognit.*, 2021, pp. 4619–4628.
- [33] X. Wang, M. H. Ang, and G. Lee, "Cascaded refinement network for point cloud completion with self-supervision," *IEEE Trans. Pattern Anal. Mach. Intell.*, vol. 44, no. 11, pp. 8139–8150, Nov. 2022.
- [34] Y. Jiang, D. Ji, Z. Han, and M. Zwicker, "SDFDiff: Differentiable rendering of signed distance fields for 3D shape optimization," in *Proc. IEEE Conf. Comput. Vis. Pattern Recognit.*, 2020, pp. 1248–1258.
- [35] Z. Han, X. Liu, Y.-S. Liu, and M. Zwicker, "Parts4Feature: Learning 3D global features from generally semantic parts in multiple views," in *Proc. 28th Int. Joint Conf. Artif. Intell.*, 2019, pp. 766–773.
- [36] Z. Han et al., "3D2SeqViews: Aggregating sequential views for 3D global feature learning by CNN with hierarchical attention aggregation," *IEEE Trans. Image Process.*, vol. 28, no. 8, pp. 3986–3999, Aug. 2019.
- [37] Z. Han, X. Wang, C.-M. Vong, Y.-S. Liu, M. Zwicker, and C. Chen, "3DViewGraph: Learning global features for 3D shapes from a graph of unordered views with attention," in *Proc. 28th Int. Joint Conf. Artif. Intell.*, 2019, pp. 758–765.
- [38] Z. Han et al., "SeqViews2SeqLabels: Learning 3D global features via aggregating sequential views by RNN with attention," *IEEE Trans. Image Process.*, vol. 28, no. 2, pp. 658–672, Feb. 2019.
- [39] Z. Han, G. Qiao, Y.-S. Liu, and M. Zwicker, "SeqXY2SeqZ: Structure learning for 3D shapes by sequentially predicting 1D occupancy segments from 2D coordinates," in *Proc. Eur. Conf. Comput. Vis.*, 2020, pp. 607–625.
- [40] Z. Han, B. Ma, Y.-S. Liu, and M. Zwicker, "Reconstructing 3D shapes from multiple sketches using direct shape optimization," *IEEE Trans. Image Process.*, vol. 29, pp. 8721–8734, 2020.

- [41] Z. Han, X. Wang, Y.-S. Liu, and M. Zwicker, "Hierarchical view predictor: Unsupervised 3D global feature learning through hierarchical prediction among unordered views," in *Proc. ACM Int. Conf. Multimedia*, 2021, pp. 3862–3871.
- [42] X. Wen, Z. Han, and Y.-S. Liu, "CMPD: Using cross memory network with pair discrimination for image-text retrieval," *IEEE Trans. Circuits Syst. Video Technol.*, vol. 31, no. 6, pp. 2427–2437, Jun. 2021.
- [43] X. Wen, Z. Han, X. Yin, and Y.-S. Liu, "Adversarial cross-modal retrieval via learning and transferring single-modal similarities," in *Proc. IEEE Int. Conf. Multimedia Expo*, 2019, pp. 478–483.
- [44] Z. Han et al., "Deep spatiality: Unsupervised learning of spatially-enhanced global and local 3D features by deep neural network with coupled softmax," *IEEE Trans. Image Process.*, vol. 27, no. 6, pp. 3049–3063, Jun. 2018.
- [45] Z. Han, C. Chen, Y.-S. Liu, and M. Zwicker, "DRWR: A differentiable renderer without rendering for unsupervised 3D structure learning from silhouette images," in *Proc. 37th Int. Conf. Mach. Learn.*, 2020, pp. 3994–4005.
- [46] X. Wen, Z. Han, G. Youk, and Y.-S. Liu, "CF-SIS: Semantic-instance segmentation of 3D point clouds by context fusion with self-attention," in *Proc. 28th ACM Int. Conf. Multimedia*, 2020, pp. 1661–1669.
- [47] X. Wen, Z. Han, X. Liu, and Y.-S. Liu, "Point2SpatialCapsule: Aggregating features and spatial relationships of local regions on point clouds using spatial-aware capsules," *IEEE Trans. Image Process.*, vol. 29, pp. 8855–8869, 2020.
- [48] X. Liu, Z. Han, X. Wen, Y.-S. Liu, and M. Zwicker, "L2G auto-encoder: Understanding point clouds by local-to-global reconstruction with hierarchical self-attention," in *Proc. 27th ACM Int. Conf. Multimedia*, 2019, pp. 989–997.
- [49] X. Liu, Z. Han, Y.-S. Liu, and M. Zwicker, "Point2Sequence: Learning the shape representation of 3D point clouds with an attention-based sequence to sequence network," in *Proc. AAAI Conf. Artif. Intell.*, 2019, pp. 8778–8785.
- [50] X. Liu, Z. Han, Y.-S. Liu, and M. Zwicker, "Fine-grained 3D shape classification with hierarchical part-view attention," *IEEE Trans. Image Process.*, vol. 30, pp. 1744–1758, 2021.
- [51] X. Liu, Z. Han, F. Hong, Y.-S. Liu, and M. Zwicker, "LRC-Net: Learning discriminative features on point clouds by encoding local region contexts," *Comput. Aided Geometric Des.*, vol. 79, 2020, Art. no. 101859.
- [52] Z. Han, X. Wang, Y.-S. Liu, and M. Zwicker, "Multi-angle point cloud-VAE: Unsupervised feature learning for 3D point clouds from multiple angles by joint self-reconstruction and half-to-half prediction," in *Proc. IEEE/CVF Int. Conf. Comput. Vis.*, 2019, pp. 10441–10450.
- [53] C. Chen, Z. Han, Y.-S. Liu, and M. Zwicker, "Unsupervised learning of fine structure generation for 3D point clouds by 2D projection matching," in *Proc. IEEE Int. Conf. Comput. Vis.*, 2021, pp. 12446–12457.
- [54] B. Ma, Z. Han, Y.-S. Liu, and M. Zwicker, "Neural-pull: Learning signed distance functions from point clouds by learning to pull space onto surfaces," in *Proc. Int. Conf. Mach. Learn.*, 2021, pp. 7246–7257.
- [55] R. Li, X. Li, C.-W. Fu, D. Cohen-Or, and P.-A. Heng, "PU-GAN: A point cloud upsampling adversarial network," in *Proc. IEEE Int. Conf. Comput. Vis.*, 2019, pp. 7203–7212.
- [56] D. Zong, S. Sun, and J. Zhao, "ASHF-Net: Adaptive sampling and hierarchical folding network for robust point cloud completion," in *Proc. AAAI Conf. Artif. Intell.*, 2021, pp. 3625–3632.
- [57] A. Dai, C. Ruizhongtai Qi, and M. Nießner, "Shape completion using 3D-encoder-predictor CNNs and shape synthesis," in *Proc. IEEE Conf. Comput. Vis. Pattern Recognit.*, 2017, pp. 5868–5877.
- [58] L. Pan et al., "Variational relational point completion network," in *Proc. IEEE/CVF Conf. Comput. Vis. Pattern Recognit.*, 2021, pp. 8524–8533.
- [59] X. Yaqi, X. Yan, L. Wei, S. Rui, C. Kailang, and S. Uwe, "ASFM-Net: Asymmetrical siamese feature matching network for point completion," in *Proc. 29th ACM Int. Conf. Multimedia*, 2021, pp. 1938–1947.
- [60] X. Yu, Y. Rao, Z. Wang, Z. Liu, J. Lu, and J. Zhou, "PoinTr: Diverse point cloud completion with geometry-aware transformers," in *Proc. IEEE/CVF Int. Conf. Comput. Vis.*, 2021, pp. 12498–12507.
- [61] W. Yuan, T. Khot, D. Held, C. Mertz, and M. Hebert, "PCN: Point completion network," in *Proc. IEEE Int. Conf. 3D Vis.*, 2018, pp. 728–737.
- [62] T. Groueix, M. Fisher, V. Kim, B. Russell, and M. Aubry, "A papier-mâché approach to learning 3D surface generation," in *Proc. IEEE Conf. Comput. Vis. Pattern Recognit.*, 2018, pp. 216–224.
- [63] S. Luo and W. Hu, "Diffusion probabilistic models for 3D point cloud generation," in *Proc. IEEE/CVF Conf. Comput. Vis. Pattern Recognit.*, 2021, pp. 2836–2844.
- [64] G. Yang, X. Huang, Z. Hao, M.-Y. Liu, S. Belongie, and B. Hariharan, "PointFlow: 3D point cloud generation with continuous normalizing flows," in *Proc. IEEE/CVF Int. Conf. Comput. Vis.*, 2019, pp. 4540–4549.
- [65] W. Yifan, S. Wu, H. Huang, D. Cohen-Or, and O. Sorkine-Hornung, "Patch-based progressive 3D point set upsampling," in *Proc. IEEE Conf. Comput. Vis. Pattern Recognit.*, 2019, pp. 5951–5960.
- [66] G. Qian, A. Abualashour, G. Li, A. Thabet, and B. Ghanem, "PGCN: Point cloud upsampling using graph convolutional networks," in *Proc. IEEE/CVF Conf. Comput. Vis. Pattern Recognit.*, 2021, pp. 11683–11692.
- [67] R. Li, X. Li, P.-A. Heng, and C.-W. Fu, "Point cloud upsampling via disentangled refinement," in *Proc. IEEE/CVF Conf. Comput. Vis. Pattern Recognit.*, 2021, pp. 344–353.
- [68] H. Fan, H. Su, and L. J. Guibas, "A point set generation network for 3D object reconstruction from a single image," in *Proc. IEEE Conf. Comput. Vis. Pattern Recognit.*, 2017, pp. 605–613.
- [69] X. Wen, J. Zhou, Y.-S. Liu, H. Su, Z. Dong, and Z. Han, "3D shape reconstruction from 2D images with disentangled attribute flow," in *Proc. IEEE/CVF Conf. Comput. Vis. Pattern Recognit.*, 2022, pp. 3793–3803.
- [70] P. Achlioptas, O. Diamanti, I. Mitliagkas, and L. Guibas, "Learning representations and generative models for 3D point clouds," in *Proc. Int. Conf. Mach. Learn.*, 2018, pp. 40–49.
- [71] D. Valsesia, G. Fracastoro, and E. Magli, "Learning localized generative models for 3D point clouds via graph convolution," in *Proc. Int. Conf. Learn. Representations*, 2019.
- [72] D. W. Shu, S. W. Park, and J. Kwon, "3D point cloud generative adversarial network based on tree structured graph convolutions," in *Proc. IEEE/CVF Int. Conf. Comput. Vis.*, 2019, pp. 3859–3868.
- [73] R. Cai et al., "Learning gradient fields for shape generation," in *Proc. Eur. Conf. Comput. Vis.*, 2020, pp. 364–381.
- [74] A. Vaswani et al., "Attention is all you need," in *Proc. 31st Int. Conf. Neural Inf. Process. Syst.*, 2017, pp. 6000–6010.
- [75] A. Dosovitskiy et al., "An image is worth 16x16 words: Transformers for image recognition at scale," in *Proc. Int. Conf. Learn. Representations*, 2021.
- [76] N. Parmar et al., "Image transformer," in *Proc. Int. Conf. Mach. Learn.*, 2018, pp. 4055–4064.
- [77] H. Zhao, L. Jiang, J. Jia, P. Torr, and V. Koltun, "Point transformer," in *Proc. IEEE/CVF Int. Conf. Comput. Vis.*, 2021, pp. 16239–16248.
- [78] M.-H. Guo, J.-X. Cai, Z.-N. Liu, T.-J. Mu, R. R. Martin, and S.-M. Hu, "PCT: Point cloud transformer," *Comput. Vis. Media*, vol. 7, no. 2, pp. 187–199, Apr. 2021.
- [79] X. Pan, Z. Xia, S. Song, L. E. Li, and G. Huang, "3D object detection with pointformer," in *Proc. IEEE/CVF Conf. Comput. Vis. Pattern Recognit.*, 2021, pp. 7463–7472.
- [80] C. R. Qi, L. Yi, H. Su, and L. J. Guibas, "PointNet: Deep hierarchical feature learning on point sets in a metric space," in *Proc. Adv. Neural Inf. Process. Syst.*, 2017, pp. 5099–5108.
- [81] C. R. Qi, H. Su, K. Mo, and L. J. Guibas, "PointNet: Deep learning on point sets for 3D classification and segmentation," in *Proc. IEEE Conf. Comput. Vis. Pattern Recognit.*, 2017, pp. 1063–6919.
- [82] X. Wen et al., "PMP-Net: Point cloud completion by transformer-enhanced multi-step point moving paths," *IEEE Trans. Pattern Anal. Mach. Intell.*, early access, Mar. 15, 2022, doi: [10.1109/TPAMI.2022.3159003](https://doi.org/10.1109/TPAMI.2022.3159003).
- [83] A. X. Chang et al., "ShapeNet: An information-rich 3D model repository," 2015, *arXiv:1512.03012*.
- [84] T. Wu, L. Pan, J. Zhang, T. Wang, Z. Liu, and D. Lin, "Balanced chamfer distance as a comprehensive metric for point cloud completion," in *Proc. Adv. Neural Inf. Process. Syst.*, 2021, pp. 29088–29100.
- [85] J. Zhang, W. Chen, Y. Wang, R. Vasudevan, and M. Johnson-Roberson, "Point set voting for partial point cloud analysis," *IEEE Robot. Automat. Lett.*, vol. 6, no. 2, pp. 596–603, Apr. 2021.

- [86] Y. Wang, D. J. Tan, N. Navab, and F. Tombari, "SoftPoolNet: Shape descriptor for point cloud completion and classification," in *Proc. Eur. Conf. Comput. Vis.*, 2020, pp. 70–85.
- [87] M. Tatarchenko, S. R. Richter, R. Ranftl, Z. Li, V. Koltun, and T. Brox, "What do single-view 3D reconstruction networks learn?" in *Proc. IEEE/CVF Conf. Comput. Vis. Pattern Recognit.*, 2019, pp. 3400–3409.
- [88] A. Geiger, P. Lenz, C. Stiller, and R. Urtasun, "Vision meets robotics: The KITTI dataset," *Int. J. Robot. Res.*, vol. 32, no. 11, pp. 1231–1237, 2013.
- [89] A. Dai, A. X. Chang, M. Savva, M. Halber, T. Funkhouser, and M. Nießner, "ScanNet: Richly-annotated 3D reconstructions of indoor scenes," in *Proc. IEEE Conf. Comput. Vis. Pattern Recognit.*, 2017, pp. 5828–5839.
- [90] X. Chen et al., "Variational lossy autoencoder," in *Proc. Int. Conf. Learn. Representations*, 2017.
- [91] D. Rezende and S. Mohamed, "Variational inference with normalizing flows," in *Proc. Int. Conf. Mach. Learn.*, 2015, pp. 1530–1538.
- [92] C. B. Choy, D. Xu, J. Gwak, K. Chen, and S. Savarese, "3D-R2N2: A unified approach for single and multi-view 3D object reconstruction," in *Proc. Eur. Conf. Comput. Vis.*, 2016, pp. 628–644.
- [93] N. Wang, Y. Zhang, Z. Li, Y. Fu, W. Liu, and Y.-G. Jiang, "Pixel2Mesh: Generating 3D mesh models from single RGB images," in *Proc. Eur. Conf. Comput. Vis.*, 2018, pp. 52–67.
- [94] L. Mescheder, M. Oechsle, M. Niemeyer, S. Nowozin, and A. Geiger, "Occupancy networks: Learning 3D reconstruction in function space," in *Proc. IEEE/CVF Conf. Comput. Vis. Pattern Recognit.*, 2019, pp. 4460–4470.
- [95] H. Xie, H. Yao, X. Sun, S. Zhou, and S. Zhang, "Pix2Vox: Context-aware 3D reconstruction from single and multi-view images," in *Proc. IEEE/CVF Int. Conf. Comput. Vis.*, 2019, pp. 2690–2698.
- [96] H. Xie, H. Yao, S. Zhang, S. Zhou, and W. Sun, "Pix2Vox : Multi-scale context-aware 3D object reconstruction from single and multiple images," *Int. J. Comput. Vis.*, vol. 128, pp. 2919–2935, 2020.
- [97] K. He, X. Zhang, S. Ren, and J. Sun, "Deep residual learning for image recognition," in *Proc. IEEE Conf. Comput. Vis. Pattern Recognit.*, 2016, pp. 770–778.
- [98] M. Berger, J. A. Levine, L. G. Nonato, G. Taubin, and C. T. Silva, "A benchmark for surface reconstruction," *ACM Trans. Graph.*, vol. 32, no. 2, pp. 1–17, 2013.



Peng Xiang received the BS degree in software engineering from Chongqing University, China, in 2019. He is currently working toward the graduate degree with the School of Software, Tsinghua University. His research interests include deep learning, 3D shape analysis, and pattern recognition.



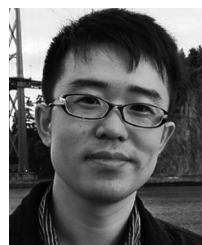
Xin Wen received the BS degree in engineering management from Tsinghua University, China, in 2012. He is currently working toward the PhD degree with the School of Software, Tsinghua University. His research interests include deep learning, shape analysis and pattern recognition, and NLP.



Yu-Shen Liu (Member, IEEE) received the BS degree in mathematics from Jilin University, China, in 2000, and the PhD degree from the Department of Computer Science and Technology, Tsinghua University, Beijing, China, in 2006. From 2006 to 2009, he was a post-doctoral researcher with Purdue University. He is currently an associate professor with the School of Software, Tsinghua University. His research interests include shape analysis, pattern recognition, machine learning, and semantic search.



Yan-Pei Cao received the bachelor's and PhD degrees in computer science from Tsinghua University, in 2013 and 2018, respectively. He is currently a principal researcher with ARC Lab, Tencent PCG. His research interests include computer graphics and 3D computer vision.



Pengfei Wan received the BE degree in electronic engineering and information science from the University of Science and Technology of China, Hefei, China, and the PhD degree in electronic and computer engineering from the Hong Kong University of Science and Technology, Hong Kong. His research interests include image/video signal processing, computational photography, and computer vision.



Wen Zheng received the bachelor's and master's degrees from Tsinghua University, Beijing, China, and the PhD degree in computer science from Stanford University, in 2014. He is currently the head of Y-tech with Kuaishou Technology. His research interests include computer vision, augmented reality, machine learning, and computer graphics.



Zhizhong Han received the PhD degree from Northwestern Polytechnical University, China, in 2017. He was a post-doctoral researcher with the Department of Computer Science, University of Maryland, College Park. Currently, he is an Assistant Professor of computer science with Wayne State University. His research interests include 3D computer vision, digital geometry processing, and artificial intelligence.

▷ For more information on this or any other computing topic, please visit our Digital Library at www.computer.org/csl.